

Radial velocities and stellar population properties of 56 MATLAS dwarf galaxies observed with MUSE

Nick Heesters¹, Oliver Müller¹, Francine R. Marleau², Pierre-Alain Duc³, Rubén Sánchez-Janssen⁴, Mélina Poulain⁵,
Rebecca Habas³, Sungsoon Lim⁶, Patrick R. Durrell⁷

¹ Institute of Physics, Laboratory of Astrophysics, École Polytechnique Fédérale de Lausanne (EPFL), 1290 Sauverny, Switzerland

² Institut für Astro- und Teilchenphysik, Universität Innsbruck, Technikerstraße 25/8, Innsbruck, A-6020, Austria

³ Observatoire Astronomique de Strasbourg (ObAS), Université de Strasbourg - CNRS, UMR 7550 Strasbourg, France

⁴ UK Astronomy Technology Centre, Royal Observatory, Blackford Hill, Edinburgh, EH9 3HJ, UK

⁵ Space Physics and Astronomy Research Unit, University of Oulu, P.O. Box 3000, FI-90014, Oulu, Finland

⁶ Department of Astronomy and Center for Galaxy Evolution Research, Yonsei University, Seoul 03722

⁷ Youngstown State University, One University Plaza, Youngstown, OH 44555 USA

Received ; accepted

ABSTRACT

Dwarf galaxies have been extensively studied in the Local Group, in nearby groups, and selected clusters, giving us a robust picture of their global stellar and dynamical properties, such as their circular velocity, stellar mass, surface brightness, age and metallicity in particular locations in the Universe. Intense study of these properties has revealed correlations between them, the so-called scaling relations, including the well known universal stellar mass-metallicity relation. However, since dwarfs play a role in a vast range of different environments, much can be learned about galaxy formation and evolution through extending the study of these objects to various locations. We present MUSE spectroscopy of a sample of 56 dwarf galaxies as a follow-up to the MATLAS survey in low-to-moderate density environments beyond the Local Volume. The dwarfs have stellar masses in the range of $M_*/M_\odot = 10^{6.1}-10^{9.4}$ and show a distance range of $D = 14-148$ Mpc, the majority (75%) of which are located in the range targeted by the MATLAS survey (10-45 Mpc). We thus report a 75% (79% for dwarf ellipticals) success rate for the semi-automatic identification of dwarf galaxies in the MATLAS survey on the here presented subsample. Using pPXF full spectrum fitting, we determine their line-of-sight velocity and can match the majority of them with their massive host galaxy. Due to the observational setup of the MATLAS survey the dwarfs are located in the vicinity of massive galaxies. Therefore, we are able to confirm their association through recessional velocity measurements. Close inspection of their spectra reveals that $\sim 30\%$ show clear emission lines and thus star formation activity. We estimate their stellar population properties (age and metallicity) and compare our results with other works investigating Local Volume and cluster dwarf galaxies. We find that the dwarf galaxies presented in this work show a systematic offset from the universal stellar mass-metallicity relation towards lower metallicities at the same stellar mass. A similar deviation is present in other works in the stellar mass range probed in this work and might be attributed to the use of different methodologies for deriving the metallicity.

Key words. Cosmology: dark matter, Cosmology: observation, Galaxies: dwarf

1. Introduction

Dwarf galaxies are regarded as the oldest and most numerous galaxy type in the Universe (Binggeli et al. 1990; Ferguson & Binggeli 1994), responsible for the formation of the more luminous and higher mass galaxies we see today (Frenk & White 2012). They are typically defined as galaxies with stellar masses $\leq 10^9 M_\odot$ (Bullock & Boylan-Kolchin 2017), small physical sizes and magnitudes fainter than -17 mag in the V -band (Tammann 1994; Tolstoy et al. 2009).

Since most dwarf galaxies have low surface brightness they are elusive when compared to massive host galaxies. Thus their study has been limited by instrumental constraints for a long time, leading to well studied populations only in the Local Group (LG; e.g., Mateo 1998; Martin et al. 2006; Ibata et al. 2007; Koposov et al. 2008; McConnachie et al. 2009; Bell et al. 2011; McConnachie 2012; Ibata et al. 2014; Martin et al. 2016; McConnachie et al. 2018; Simon 2019; Drlica-Wagner et al. 2020) and a handful of nearby groups in the Local Volume (LV; $D \leq 10$ Mpc) (e.g., Chiboucas et al. 2013; Danieli et al. 2017; Crnojević et al. 2019; Carlsten et al. 2019; Bennet et al. 2020; Müller

et al. 2021), and some galaxy clusters (e.g., Ferrarese et al. 2012; Eigenthaler et al. 2018; Venhola et al. 2019). In order to model and understand galaxy formation and evolution across cosmic time, it is essential to answer the question of whether the dwarfs studied in the Local Volume are representative of dwarfs in the nearby Universe at large.

Even though galaxy formation and evolution is thought to depend on a number of different factors and processes, galaxies show remarkably tight correlations between some of their basic stellar and dynamical properties (e.g., Binggeli & Jerjen 1997; Tassis et al. 2008). These so-called scaling relations have been extensively studied for different galaxy types, in a range of environments, and in particular in light of a possible evolution with time (see e.g., D’Onofrio et al. 2021, for a recent review). A few examples of well established galaxy scaling relations are the velocity-luminosity or Tully-Fisher relation (Tully & Fisher 1977; Courteau et al. 2007), the Faber-Jackson relation (Faber & Jackson 1976), the Kormendy relation (Kormendy 1977), the fundamental plane of galaxies (e.g., Djorgovski & Davis 1987; Dressler et al. 1987; Cappellari et al. 2006; La Barbera et al.

2008), the bulge to black hole mass relation (Magorrian et al. 1998) and the mass-radius relation (Chiosi et al. 2020).

The mass-metallicity relation (MZR) is another long known and studied scaling relation which exists for both gas- and stellar metallicities (see e.g., Maiolino & Mannucci 2019, for a recent review). Stellar spectroscopy and the analysis of color-magnitude diagrams first revealed this connection in nearby elliptical galaxies (McClure & van den Bergh 1968; Sandage 1972; Mould et al. 1983; Buonanno et al. 1985). Analysis of the Sloan Digital Sky Survey (SDSS) optical spectra has shown that this relation persists in galaxies with stellar masses in the range $M_*/M_\odot = 10^9$ - 10^{12} for stellar and gas metallicities (Tremonti et al. 2004; Gallazzi et al. 2005, 2006; Lee et al. 2006; Panter et al. 2008; Mannucci et al. 2010; González Delgado et al. 2014). The study of this correlation was extended to dwarf galaxies in the LG, where Kirby et al. (2013) found that dwarf galaxies follow the same stellar MZR as more massive galaxies. This result was also found in semi-analytical galaxy formation and evolution models (SAMs) by several authors (e.g., Li et al. 2010; Font et al. 2011; Hou et al. 2014; Lu et al. 2014, 2017). Xia & Yu (2019a,b) have demonstrated that the relation is universal in SAMs for different types of galaxies and over a large range of stellar ($M_*/M_\odot \sim 10^3$ - 10^{11}) and dark matter halo masses ($M_{\text{halo}}/M_\odot \sim 10^9$ - $10^{15} h^{-1}$).

There are various mechanisms which are potentially driving the MZR and have been discussed in the literature (see Maiolino & Mannucci 2019, and references therein). The most important ones are: outflows due to stellar feedback (e.g., Garnett 2002; Brooks et al. 2007), downsizing (e.g., Cowie et al. 1996), low mass galaxies being in an earlier evolutionary stage and therefore showing larger gas fractions (e.g., Erb et al. 2006), a potentially mass-dependent initial mass function for higher mass galaxies (e.g., Köppen et al. 2007; Trager et al. 2000; Mollá et al. 2015; Vincenzo et al. 2016; Lian et al. 2018) and finally metal-rich accreted gas from previous burst of star formation in larger mass systems compared to lower mass ones (Brook et al. 2014; Ma et al. 2016).

In addition to the mass of a galaxy, its environment is one of the main independent factors when it comes to galaxy evolution and as such has been studied extensively in the context of the MZR (Trager et al. 2000; Kuntschner et al. 2001; Thomas et al. 2005, 2010; Sheth et al. 2006; Sánchez-Blázquez et al. 2006; Pasquali et al. 2010; Zhang et al. 2018). It has been found that while the environment has a significant influence on the morphology, age and star formation activity of a galaxy, its direct contribution to the shape of the MZR is small (Thomas et al. 2010; Mouhcine et al. 2011; Fitzpatrick & Graves 2015; Sybilka et al. 2017). Peng et al. (2015) and Trussler et al. (2020), however, find that dwarf satellite galaxies in high density environments are more metal rich compared to dwarfs residing in lower density environments. This observation is attributed to the process of starvation, i.e., the lack of cold gas accretion in these high density regions.

One caveat when calculating the MZR and comparing with results from other works is the variety of methods which can be used to determine the metallicity (e.g., Kewley & Ellison 2008). Another important factor in the context of this work is that there have been few studies investigating the MZR in the dwarf galaxy mass regime (Lequeux et al. 1979; Lee et al. 2006; Vaduvescu et al. 2007; Zahid et al. 2012; Kirby et al. 2013; Andrews & Martini 2013) and these have mostly been limited to the LG. Therefore, increasing the sample size of dwarf galaxies in different environments will greatly benefit these discussions. In recent years there has been a great effort to advance our knowledge

of dwarf galaxies beyond the boundaries of the LG (e.g., Irwin et al. 2009; Stierwalt et al. 2009; Kim et al. 2011; Chiboucas et al. 2013; Bennet et al. 2017; Danieli et al. 2017; Park et al. 2017; Cohen et al. 2018; Crnojević et al. 2019; Müller & Jerjen 2020; Davis et al. 2021; Drlica-Wagner et al. 2021; Müller et al. 2021; Mutlu-Pakdil et al. 2022; Carlsten et al. 2022) and further beyond the LV (e.g., Geha et al. 2017; Greco et al. 2018; Zaritsky et al. 2019; Habas et al. 2020; Su et al. 2021; Prole et al. 2021; Tanoglidis et al. 2021; Mao et al. 2021; La Marca et al. 2022). The MATLAS survey (Duc et al. 2015; Bílek et al. 2020), the basis for this study, is among the latter and delivers a large number (2210) of newly discovered dwarf galaxies beyond the LV. The vast majority of the dwarf galaxies identified in the MATLAS fields around ~ 140 targeted ETGs, however, only have photometric data and thus their distance, satellite nature and environment is uncertain. In the case of the M101 group, in the Local Volume, it has been shown that $\sim 80\%$ of the candidates in a dwarf catalog have been contaminants (Bennet et al. 2017, 2019). However, due to a careful detection and selection procedure (see Habas et al. 2020), the degree of contamination in the MATLAS dwarf catalog is likely significantly lower. In order to advance our understanding of structure formation as a function of the environment, it is therefore of great importance to obtain distance or recessional velocity estimates for dwarf galaxies in order to confirm their dwarf and satellite nature.

In this study we aim to add information about line-of-sight velocities of dwarf galaxies identified in the MATLAS fields beyond the LV and to compare their extracted stellar population properties with results from other studies. This information contributes to the connection between host halo and number of subhalos (e.g., Kim et al. 2018; Nadler et al. 2019; Munshi et al. 2021), the morphology-density relation, i.e. the role the environment plays in the formation and evolution of dwarf galaxies (e.g., Ferguson et al. 1990; McConnachie 2012; Ferguson & Sandage 1989; Sawala et al. 2012; Steyrleithner et al. 2020), the discussion on phase-space correlations in dwarf satellites (e.g., Kunkel & Demers 1976; Lynden-Bell 1976; Pawlowski et al. 2012; Ibata et al. 2013; Müller et al. 2016, 2018, 2019, 2021; Heesters et al. 2021; Sawala et al. 2022) and the study of scaling relations for low-mass galaxies beyond the LV (see Habas et al. 2020; Poulain et al. 2021; Marleau et al. 2021; Poulain et al. 2022, on scaling relations in the MATLAS dwarfs based on photometry).

This paper is structured as follows: in Section 2 we describe the MATLAS survey as a precursor and base for this study, as well as the observational details utilizing the MUSE instrument. We then map out the individual steps we use to reduce the data, to fit the spectra and to estimate our errors. In Section 3 we present our findings regarding the dwarf line-of-sight velocities and resulting satellite nature. We then discuss background contamination as mentioned above and comment on the assumptions regarding satellite membership made in the MATLAS survey. We extract the stellar populations and discuss our results in light of the universal stellar mass-metallicity relation. In Section 4 we summarize our results and give an outlook.

2. Observations and data reduction

2.1. The MATLAS dwarf galaxy candidate sample

The dwarf galaxies were identified (Habas et al. 2020) in the MegaCam images of the MATLAS survey (Duc et al. 2015), an extension of the ATLAS^{3D} project (Cappellari et al. 2011), which aims to characterize the morphology and the kinematics of 260 early-type galaxies (ETG) in the context of galaxy for-

mation and evolution. The ETGs are between 10 and 45 Mpc, have declinations within $|\delta - 29| < 35$ degrees, galactic latitudes > 15 degrees, and K -band absolute magnitudes below -21.5 . The hosts mostly reside in group environments and a few are isolated.

The MATLAS fields were observed between 2012 and 2015. Each pointing has an ETG in its center and may contain additional ETGs and late-type galaxies. The MATLAS data was observed in the g , r , and i -bands for 150, 148, and 78 fields, respectively, as well as in the u -band for 12 fields. A surface brightness limit of $28.5 - 29.0$ mag arcsec $^{-2}$ was reached in the g -band.

In total 2210 dwarf galaxies were identified in these fields using a visual and semi-automatic approach (Habas et al. 2020). Their structural parameters were presented in Poulain et al. (2021). About 75 % of the dwarf galaxy candidates are dwarf ellipticals (dEs). The dwarfs are located in 1 deg 2 fields around the targeted ETG with a median value of 17 dwarf galaxies per field (see Habas et al. 2020, for details on the MATLAS dwarf catalog). Since there are no distance estimates for the majority (~ 85 %) of the dwarfs and the fields often contain massive ETGs and/or LTGs in addition to the targeted ETG, the satellite nature and association of the dwarfs to the massive galaxies are uncertain. In Habas et al. (2020), distances were estimated for 14 % based on literature spectroscopic and HI measurements (Poulain et al. 2022), of which 90 % were confirmed to be members of the host system based on their relative velocities being consistent with the hosts velocity. Out of the 2210 dwarf galaxies, 3 % fall into the regime of the ultra-diffuse galaxies (Marleau et al. 2021). Based on their globular cluster count, one of the most extreme cases of these ultra-diffuse galaxies is MATLAS-2019, which has been observed with HST (Müller et al. 2021; Danieli et al. 2022) and MUSE (Müller et al. 2020). Based on the MUSE observations, it has a metal-poor and old stellar population (Müller et al. 2020).

2.2. MUSE observations

In this work, we followed up 56 dwarf galaxies from the MATLAS survey. We obtained the data from the Multi Unit Spectroscopic Explorer (MUSE; Bacon et al. 2010, 2012) at the Very Large Telescope (VLT) of the European Southern Observatory (ESO) from four different proposals and observational periods: P103 (PI: Marleau, proposal ID: 0103.B-0635), P106 (PI: Marleau, proposal ID: 106.21A1), P108 (PI: Marleau, proposal ID: 108.2214) and P109 (PI: Marleau, proposal ID: 109.22ZV). The goal of these proposals was to obtain a reference sample of dwarf galaxies identified in the low-to-moderate density MATLAS fields and the galaxies were observed under relaxed seeing conditions (filler conditions), with an average seeing of 1.0 arcsec. We selected our targets to have an average surface brightness $\langle \mu_{e,g} \rangle < 25.5$ mag/arcsec 2 in the g -band and an effective radius $r_{eff} > 3$ arcsec. All targets satisfy $2r_{eff} < 1$ arcmin and are thus well matched with the field of view (FOV) of the MUSE Wide Field Mode (WFM) of 1×1 arcmin 2 with a spatial sampling of 0.2×0.2 arcsec 2 . The instrument covers a spectral range of 4750-9350 Å with a sampling of 1.25 Å and a resolving power of 1770 (480 nm) - 3590 (930 nm). Each galaxy was observed for a single Observational Block (OB) with four science exposures (O) amounting to an on-target integration time of 2700 s. We chose an OOOO observing sequence with 90 degree rotations and small dithering. The size of the galaxies in relation to the MUSE FOV allows us to obtain the sky spectra directly from the science exposure by implementing an offset

from the target of $\pm \sim 10$ arcsec in right ascension (RA) and declination (Dec). All of our targets are thus situated in a corner of the MUSE FOV, so as to optimize sky exposure and minimize contamination from stars and background galaxies. This strategy was used in other works in the literature (e.g., Emsellem et al. 2019; Fensch et al. 2019; Müller et al. 2020).

2.3. Sky subtraction

In order to enhance the sky subtraction performed in the reduced MUSE data cubes by the ESO pipeline, we first use the MUSE Python Data Analysis Framework (MPDAF) to collapse the data cube along the wavelength axis. We then detect all sources in the produced 2D image and create a binary mask, with 1 corresponding to a detection and 0 to the background. For this task we use a combination of Source Extractor (Bertin & Arnouts 1996) and MObjects (Teeninga et al. 2015), employing their respective strengths of detecting faint point sources (Source Extractor) and the low surface brightness galaxy itself (MObjects). This mask is used as an input for the Zurich Atmosphere Purge (ZAP; Soto et al. 2016) developed for MUSE, which uses principal component analysis in order to isolate and subtract sky features from the data cube.

2.4. Spectral extraction

To extract the galaxies' spectra, we create masks for all of the dwarf galaxies on an individual basis, in order to isolate the dwarf spectra from the ones coming from other sources in the field of view. We use a combination of Source Extractor and manual masking in order to eliminate bright sources. Depending on the shape of the dwarf we draw circular or elliptical apertures centered on the galaxy. The resulting mask contains values 1 for the dwarf flux and 0 in all other regions, i.e., for radii beyond the defined aperture, where the collapsed image contains bright sources and where the median flux has values $\leq 0.2 * 10^{-20}$ erg/(Å cm 2 s). The latter constraint aids the optimization of the signal-to-noise ratio (SNR) per spaxel. We extract the noise from the second extension of the MUSE data cube using the same mask. In addition to a spatial mask, we also create a spectral one, manually eliminating residual sky lines which are not considered in the following full spectrum fitting (see the gray bands in Figure 1).

2.5. Full spectrum fitting

We fit the dwarf galaxy spectra using the Penalized Pixel-Fitting algorithm (pPXF; Cappellari & Emsellem 2004; Cappellari 2017), a standard full spectrum fitting method to extract stellar and gas kinematics as well as stellar populations. Employing a similar strategy as in the literature (e.g., Emsellem et al. 2019; Fensch et al. 2019; Müller et al. 2021; Fahrion et al. 2022), we use single stellar population (SSP) models from the E-MILES library (Vazdekis et al. 2016) with ages ranging from 70 Myr to 14 Gyr and metallicities from solar down to -2.27 dex. We use a Kroupa initial mass function (IMF; Kroupa 2001) and account for the slightly varying MUSE resolution across the spectral range by convolving with a MUSE line spread function as described in Guérou et al. (2017). In order to extract the line-of-sight velocities we use additive and multiplicative polynomials of degrees 8 and 12, respectively (Emsellem et al. 2019). For the stellar population properties age and metallicity we fix the determined velocity and rerun pPXF, using only multiplicative

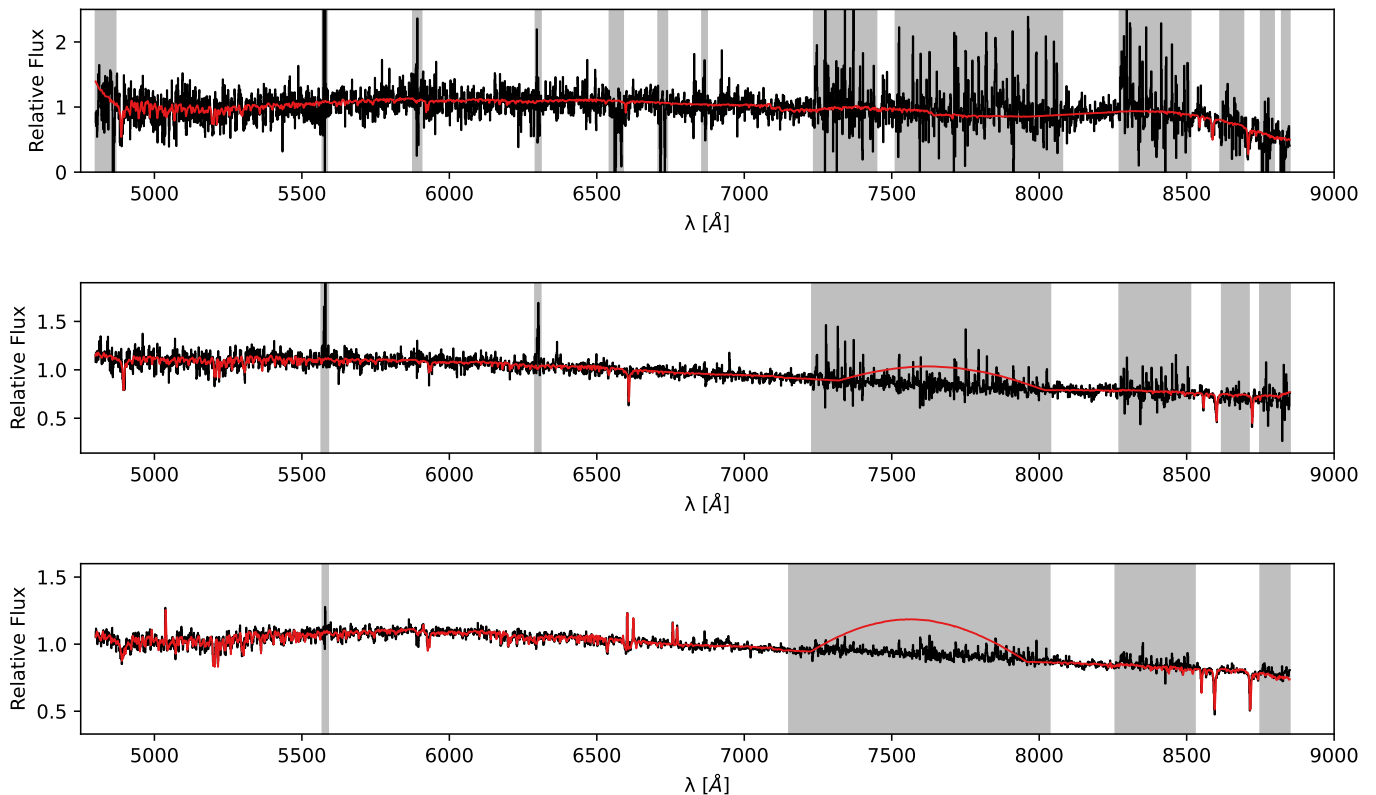


Fig. 1: Examples of different quality, i.e., different SNR, spectra. We show the relative flux on the y-axis and the wavelength on the x-axis in angstroms. We note that these spectra have not been shifted to the rest frame. The black line is the galaxy spectrum and the red line the fit produced by pPXF. Gray regions were manually masked out to improve the fit. From top to bottom we show the spectra for the galaxies MATLAS-269, MATLAS-1232 and MATLAS-10 with SNRs of 8.7, 26.0 and 61.9, respectively.

polynomials of degree 12 (Fensch et al. 2019). In dwarf galaxies featuring emission lines, we determine the line-of-sight velocity by fitting absorption and emission lines simultaneously. For the stellar populations we first mask all emission lines, only leaving the absorption spectrum. We utilize the weights returned by pPXF to calculate the mean age and metallicity as well as the mass-to-light ratio (ML) in the V -band from the E-MILES SSPs for each galaxy. Here the ML is not a fitted parameter such as age and metallicity but is rather inferred from the age and metallicity grid returned by pPXF.

2.6. Signal-to-noise ratio optimization

The dwarf galaxies in this sample show a wide variety of SNRs. In Figure 1 we show examples of different quality dwarf spectra (i.e., different SNRs). The black lines show the galaxy flux while the red ones are the best fit lines returned by pPXF. Gray regions were manually masked and are not considered in the fit. This can lead to curves in the fit line in these unconstrained regions. An example of this can be seen in the second and third spectra in Figure 1 in the grayed out region ($\sim 7200\text{--}8000 \text{ \AA}$). This does, however, not affect the quality of the fit.

In order to gain the maximal value from our MUSE data, we select the aperture from which we extract the spectrum so that the signal-to-noise ratio is optimized. To do this, we use the center of the dwarf galaxy and perform pPXF fitting for increasing aperture radii in a range $r \in [10, 100]$ pix in steps of 10 pix. We choose this range based on the apparent sizes these dwarfs have

in the MUSE image ($\sim 300 \times 300$ pix). We use the aperture at the peak of the SNR to extract the spectrum and proceed with the analysis. To illustrate the difference between the spectrum extracted using a visually intuited aperture and the SNR optimized one, we show the corresponding spectra for one of the dwarfs (MATLAS-445) in Figure 2. As is done in other studies (e.g., Fahrion et al. 2019a; Müller et al. 2020; Fahrion et al. 2020; Müller et al. 2021), we calculate the SNR in a region of the spectrum featuring no strong absorption or emission lines. Other works (e.g., Fahrion et al. 2019a; Müller et al. 2021) have used the wavelength interval $[6600, 6800] \text{ \AA}$ for this purpose. Since the dwarf galaxies analyzed in this work show a range of different redshifts, we use this wavelength interval and shift it using the estimated redshift for each galaxy via the best fit recessional velocity. The SNR is calculated as the mean fraction between the flux and the square root of the variance. For this, the variance is multiplied by the χ^2 value returned by pPXF, thus using a better estimate for the local noise (Fensch et al. 2019; Müller et al. 2020).

For galaxies which are best described by an elliptical aperture, we increase its size by varying the semi-major axis $a \in [10, 100]$ and keeping the axis ratio between minor and major axis of the ellipse constant. We use the radius or semi-major axis a for which the SNR peaks for all further analysis. In some instances the SNR does not show a peak in the tested interval but diverges. Individual inspection of these cases reveals that this only occurs in low SNR ($\lesssim 10$) and very faint galaxies. In these cases we manually set the aperture to best match visual intuition

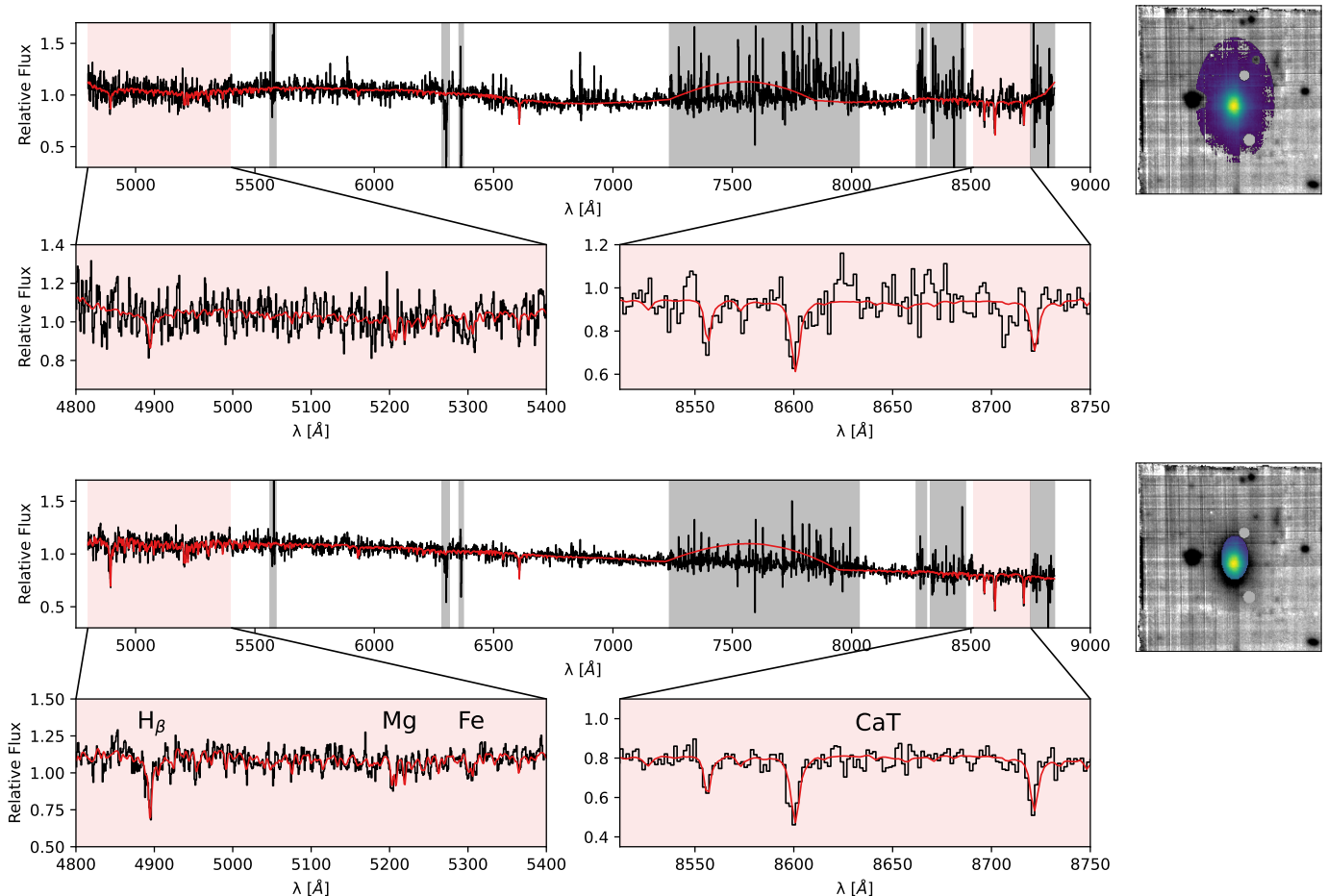


Fig. 2: Comparison of dwarf spectra from visually intuited aperture (top) vs. SNR optimized aperture (bottom). Right: stacked MUSE cube of the dwarf MATLAS-445. The spectra were extracted from the colored regions. The SNR was improved from 29.3 (visually intuited aperture) to 32.4 (optimized aperture) for this galaxy.

from the stacked data cube. It should be noted that for nucleated dwarfs we masked the nucleus for this SNR optimization in order to avoid a bias towards smaller apertures due to the nucleus dominating the SNR. We subsequently unmask the nucleus when extracting the dwarf properties.

In the top panel of Figure 3 we show the SNR distribution of all dwarfs in our sample, which takes values in the range $\sim[5,63]$. In the bottom panel of the same figure we show the distribution of apertures (radius or semi-major axis) which lead to the maximum SNR for our dwarf sample and relate these apertures to the effective radius from their GALFIT model (Habas et al. 2020; Poulain et al. 2021). We can see a prominent peak around ~ 5 arcsec. In the top panel of Figure 4 we see that the effective radius r_{eff} roughly traces the SNR optimized aperture. However, with a rather large scatter, which increases significantly as the dwarf size increases. Since we have obtained profiles describing the SNR as a function of the radius and have similar profiles of the surface brightness (measured in the g -band) as a function of the radius (see Poulain et al. 2021), we can relate the SNR with the surface brightness. In the bottom panel of Figure 4 we show the distribution of the surface brightness at the SNR optimized dwarf radius. For eight dwarfs the SNR curve diverged and we set the optimal aperture manually at the first peak (if applicable) or based on visual intuition. We omit these dwarfs from the plot. In a few cases we are not able to obtain the surface brightness profile from the MATLAS images directly and measure it

on the dwarf's GALFIT model. These cases are shown in blue. We note a clear peak at ~ 25.5 mag arcsec $^{-2}$ and a second smaller one at ~ 20 mag arcsec $^{-2}$. Out of these 11 dwarfs in the lower peak, 8 show strong emission lines, which may explain the optimal radius at such high surface brightnesses. This distribution illustrates the gains expected in terms of SNR by probing deeper surface brightnesses.

2.7. Error estimation

We estimate the errors for all properties by running a Monte Carlo (MC) simulation. We determine the best fit to the galaxy spectrum using pPXF and calculate the residuals between best fit and input spectrum at each wavelength. We then create new realizations of the spectrum by using the best fit as a base line. At each wavelength we randomly add the residual or subtract it from the best fit. We re-run pPXF for the newly generated spectrum and compare the original values for the radial velocity, age and metallicity with the returned values for the new realization. We repeat this 400 times for each galaxy. This number is motivated by the error estimation for the lowest SNR galaxy in our sample for which a recession velocity is obtainable. We varied the number of MC runs in an interval $N_{MC} \in [100, 1000]$ in steps of 100 for this galaxy and observed stable values after 400 runs. The 1σ confidence interval of these MC simulations give the errors for each extracted property. We use the value of the

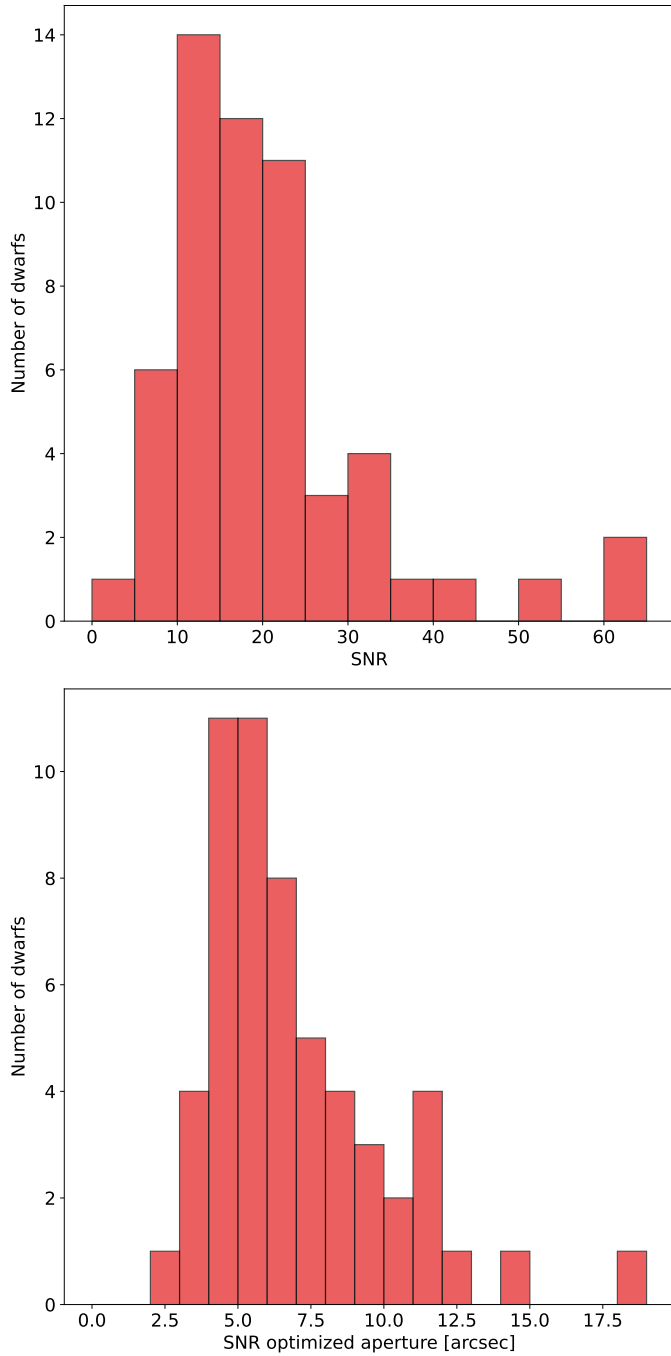


Fig. 3: Distributions of signal-to-noise ratios and corresponding SNR optimized apertures from which the spectra were extracted. Top: distribution of SNRs for the sample of dwarf galaxies analyzed in this work. Bottom: distribution of SNR optimized apertures for the dwarf galaxies studied in this work.

initial best fit and calculate the errors in relation to the MC 1σ interval. In case the best fit value lies outside of this interval (see Figure 5), we use the mean and 1σ bounds of the MC simulation. In Appendix A we show the residuals of the best fit value (velocity, age and metallicity) minus the mean/median of the respective MC realizations and indicate whether the best fit values lie within or outside the 1σ from the MC simulation. While overall the best fit values are consistent with the mean and median of

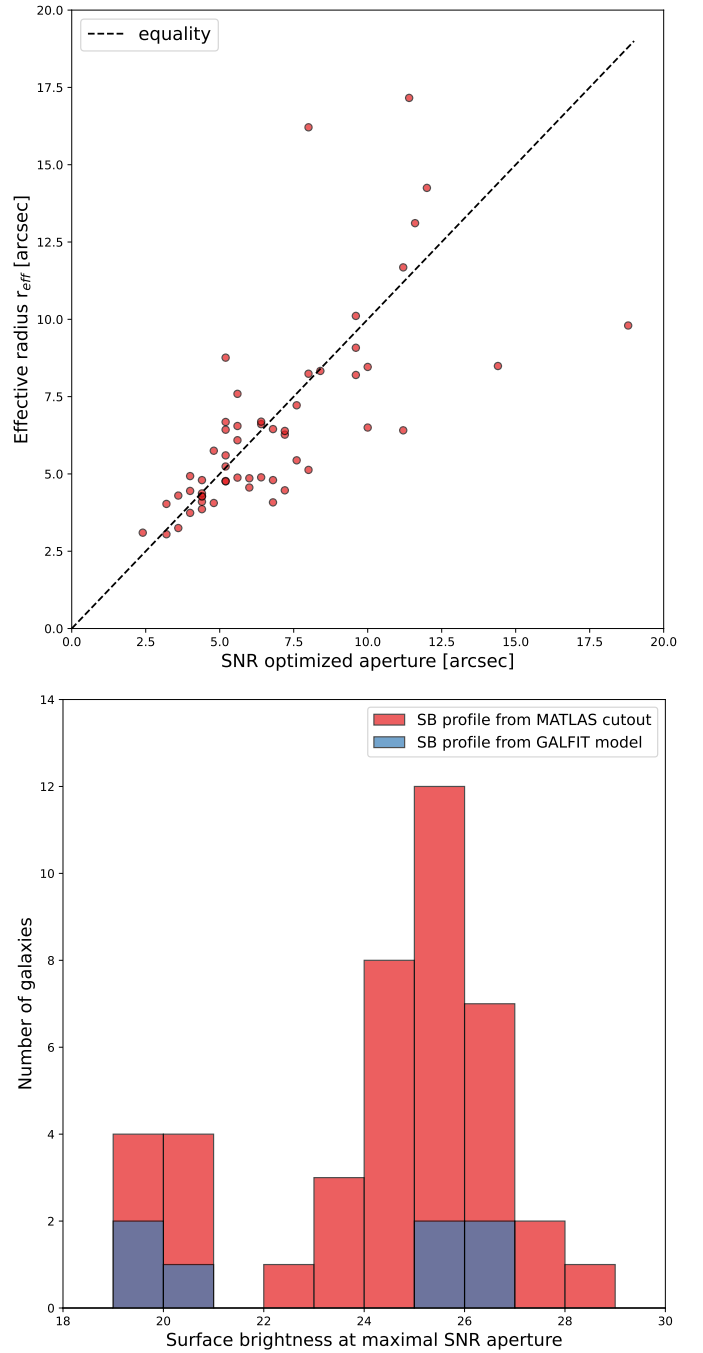


Fig. 4: Comparison of photometric properties with the SNR optimized apertures. Top: comparison between the SNR optimized radius obtained in this work and the effective radius from Poulain et al. (2021). The black dashed line indicates the equality of the two measurements. Bottom: distribution of the dwarf g -band surface brightness from Poulain et al. (2021) at the radius which optimizes the SNR of the extracted spectrum.

the MC realizations, there are some cases where the two values differ, in particular for the age.

3. Results and discussion

In the following, we present the results of our analysis of the 56 non-cluster dwarf galaxies and compare them against dwarfs

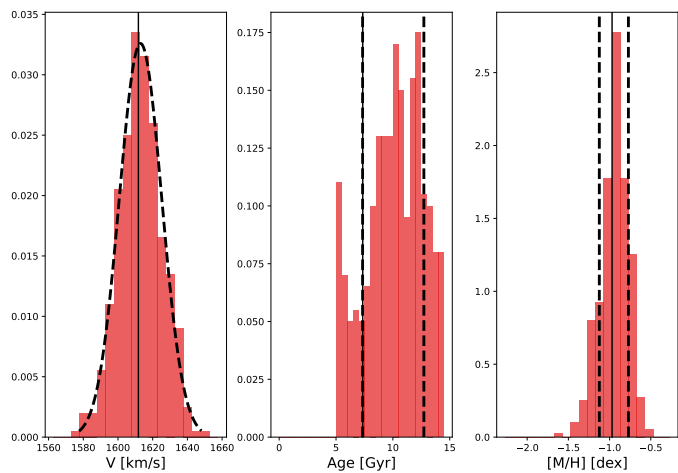


Fig. 5: Results from the MC error estimation with 400 iterations for the galaxy MATLAS-269. The histograms show the distributions of the fit values for the recessional velocity V , the age and the metallicity obtained from pPXF by randomly flipping the sign of the residual between the galaxy spectrum and the initial best-fit. The solid lines indicate the best-fit values of the original spectrum while the dashed lines show the standard deviation of the MC realizations. For the recessional velocity shown in the leftmost panel, we fit a Gaussian curve (dashed line) to the distribution of MC realizations.

in the literature. First, we discuss the line-of-sight velocities obtained from the MUSE spectra and relate this new information to the assumptions made in the MATLAS studies (e.g., Habas et al. 2020; Poulain et al. 2021; Marleau et al. 2021; Heesters et al. 2021; Poulain et al. 2022). Next, we illustrate the photometric properties of the subsample of MATLAS dwarfs observed with MUSE in relation to the MATLAS sample as a whole. We then examine the stellar population properties metallicity and age of this sample and compare with dwarf properties from other works. We summarize the derived properties of the dwarf sample studied in this work in Table A.1 in the Appendix A.

3.1. Line-of-sight velocity

We obtain recessional velocity estimates from all but four galaxies ($\sim 7\%$) in our sample, for which the SNR is too low to identify or fit any spectral lines. The distribution of these velocities is shown in Figure 6. The bulk of our sample ($\sim 75\%$) shows velocities in an interval $[1000, 3000]$ km/s. This is consistent with the distance probed by the MATLAS survey of ~ 10 -45 Mpc with line-of-sight velocities $\in [-300, 3800]$ km/s. The dwarf galaxies in this velocity interval match well with the recessional velocities of nearby massive galaxies targeted in the ATLAS^{3D} survey. The semi-automatic dwarf identification approach described in Habas et al. (2020) thus shows a success rate of 75% (79% for the dEs) on this sample. We note that these numbers are lower limits for our dwarfs, since the four dwarfs for which we could not obtain a velocity estimation may still be satellites of nearby host galaxies and were classified as non-satellites for the sake of this calculation. We find that 10 dwarf galaxies identified in the MATLAS fields, and previously assumed satellites of the respective targeted ETG in the field, show velocities which are inconsistent with any host in the distance range probed by ATLAS^{3D}. These appear to lie further in the background. We note that 7 out of these 10 galaxies show strong emission lines, indicating on-

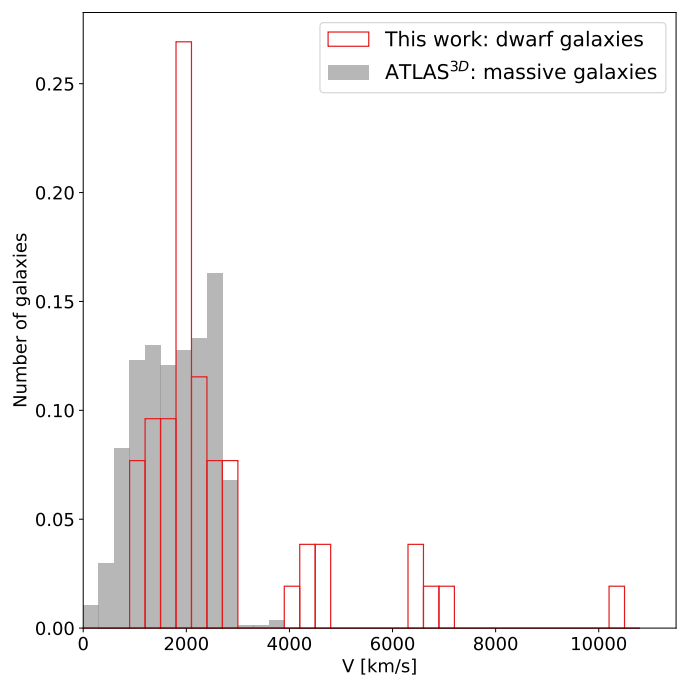


Fig. 6: Distribution of the measured dwarf line-of-sight velocities studied in this work. The first peak corresponds to the velocity space which is consistent with the hosts targeted in the ATLAS^{3D} survey.

going star formation. We would expect such a correlation, since star forming objects appear brighter and are thus detectable in our fields, whereas distant quiescent ones may largely be too faint and thus elusive in this context. Another reason for this correlation is likely connected to the selection process of the MATLAS dwarfs during which a size cut was applied in order to remove background objects. Background dwarfs which remain in the sample after this cut are likely to be on the high end of the mass range (see Figure 10) and have a higher reservoir of gas and dust for star formation. Furthermore, star forming objects are challenging to classify and distance estimation based on visual intuition through surface brightness fluctuation is inapplicable for such objects.

We match the dwarf recessional velocities with the one of nearby ATLAS^{3D} host galaxies and declare them satellites of the host with the smallest velocity difference $\Delta V = V_{sat} - V_{host}$. We find a maximal $\Delta V_{max} = 460$ km/s and a maximal projected separation between host and satellite of $\Delta d_{max} = 391$ kpc. There is a clear gap in the velocity distribution shown in Figure 6, between the dwarfs matching with hosts in the probed MATLAS distance range (first peak) and background dwarfs. We reassign the dwarfs from the assumed host in the MATLAS studies (targeted ETG in each field) to new hosts according to their best ΔV match and show the results of this procedure in Figure 7. We plot the projected distance between satellite and host in kpc on the x-axis and the difference in recessional velocities on the y-axis. The gray circles indicate the values following the MATLAS assumptions, which are shifted (gray arrows) towards the red points by assigning a better matching host galaxy with the new spectral information. For red points circled in grey the assumed MATLAS host does not change with new velocity information. We mark the ± 300 km/s boundaries as dashed lines, which is a typical relative velocity cut for satellite populations. This is, however, not a strict cutoff as greater velocity dispersions are

possible in group environments. If we instead adopt a cut of $\Delta V \sim 500$ km/s as is done in Habas et al. (2020), all of our matched dwarfs lie within.

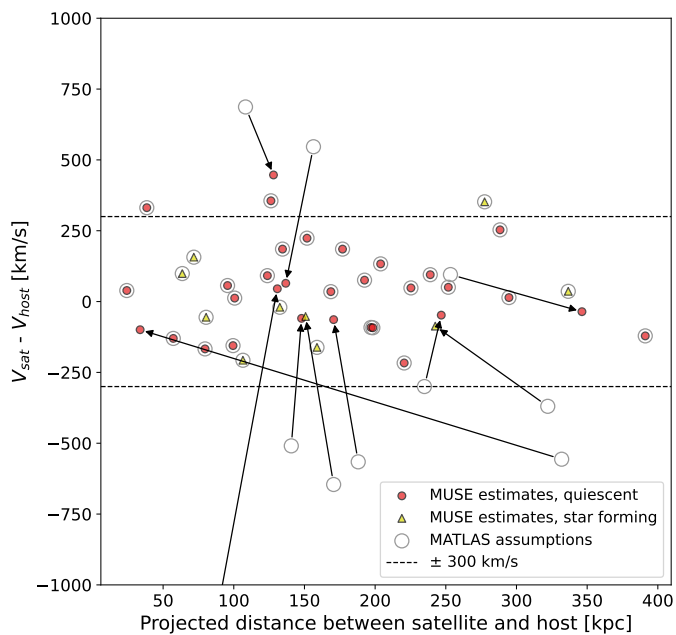


Fig. 7: Projected distance between satellite and assumed host galaxy in kpc vs recessional velocity difference between satellite and host ($\Delta V = V_{sat} - V_{host}$) in km/s. We plot the projected distance and velocity difference to the host assumed in MATLAS (grey circles) compared with the updated host based on minimal ΔV through MUSE spectral fitting (red). These shifts are indicated by grey arrows. For red points circled in grey the assumed host stays the same with new velocity information on the dwarf. The dashed black lines show ± 300 km/s.

3.2. Photometric properties

In order to illustrate whether our MATLAS subsample with MUSE observations is representative of the MATLAS sample overall, we compare their photometric properties from GALFIT (Peng et al. 2002, 2010) modeling (see Habas et al. 2020 and Poulain et al. 2021) in Figure 8. We show the Sersic index, the g -band apparent magnitude m_g , the effective radius r_{eff} in arcsec and the axis ratio. The MATLAS sample consisting of 1589 dwarfs with successful GALFIT models and reliable r_{eff} estimates is shown in gray, the subsample with MUSE observations is in red. Both samples are displayed normalized for improved visibility. The samples overlap well in general. We note a shift towards brighter magnitudes and larger effective radii for the MUSE sample. This is caused by our observational selection criteria, which are in place to ensure sufficient SNR for our main objectives in a single OB. We note that there are no Ultra Diffuse Galaxies (UDGs), i.e., dwarfs with excess effective radius in our MUSE sample.

We show the scaling relation absolute magnitude M_g vs effective radius r_{eff} in Figure 9 (see also Habas et al. 2020; Poulain et al. 2021; Marleau et al. 2021; Poulain et al. 2022). Since there are no distance or velocity estimates for the majority of the MATLAS dwarfs, M_g was estimated by assuming the distance of central ETG of the field the dwarf appears in. A portion of the dwarf galaxies ($\approx 15\%$) has a distance or velocity estimate from other

surveys, in which case we use this estimate. For the MUSE sample we use the distance of the massive galaxy which best matches the MUSE estimate in terms of line-of-sight velocity. These host distances are taken from the ATLAS^{3D} survey and are mostly based on redshift and surface brightness fluctuation (SBF) measurements (see Cappellari et al. 2011a). For dwarfs which are not satellites of any host in the ATLAS^{3D} catalog, we use the recessional velocity obtained via MUSE spectroscopy and transform it into the distance space via Hubble's law $D = V/H_0$. Here, D denotes the distance to the dwarf, v the line-of-sight velocity and H_0 the Hubble constant ($H_0 = (69.8 \pm 1.7)$ km/s/Mpc; Freedman 2021). There is no notable difference between the subsample with MUSE observations (red) and the full MATLAS sample (gray) with GALFIT models. We therefore conclude that our MUSE sample is representative of the dwarf galaxies identified in the MATLAS survey.

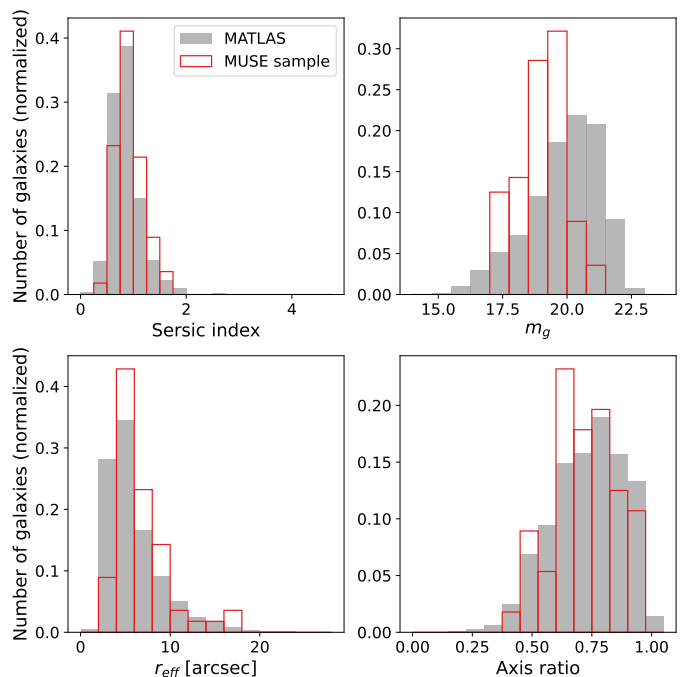


Fig. 8: Photometric properties of the MATLAS sub-sample targeted with MUSE (red) compared with the overall distribution of the MATLAS dwarf galaxies (grey) with robust GALFIT modelling. Top left: Sersic index, top right: apparent g -band magnitude m_g , bottom left: effective radius r_{eff} and bottom right: axis ratio.

3.3. Stellar populations

Dwarf galaxies in the Local Universe follow the universal stellar mass-metallicity relation (Kirby et al. 2013). In order to relate our data to this observation, we estimate the stellar mass M_* of our dwarf galaxies by first transforming the apparent g -band magnitude m_g from Poulain et al. (2021) to the V -band by using the transformation equation from Lupton (2005):

$$V = g - 0.5784 * (g - r) - 0.0038 \quad (1)$$

and use the $g-r$ colors from Poulain et al. (2021). For the galaxies without $g-r$ values from GALFIT, we use the $g-r$ estimates from Source Extractor on the MATLAS images by using an aperture of $3r_{eff}$. We then transform the apparent V -band

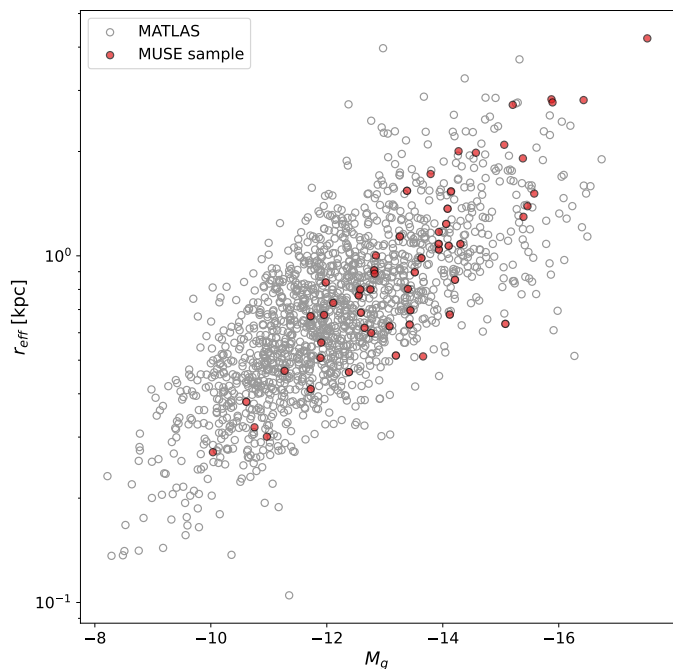


Fig. 9: Scaling relation absolute g -band magnitude M_g vs effective radius r_{eff} in kpc. Comparison between the dwarf sample studied in this work (red) and the overall MATLAS sample (grey). To get these measurements for the sample with MUSE observations we use the distance of the associated host galaxy and if not available we use the dwarf velocity to estimate the distance via Hubble’s law.

magnitude to the absolute magnitude M_V . For this we estimate the distance to the dwarf galaxy as described in Section 3.2. Finally, we convert the absolute magnitude M_V to L_V and use the stellar mass-to-light estimate from pPXF to estimate the stellar mass M_* .

In Figure 10 we present the results from our sample (red) and compare it with the relation shown in Kirby et al. (2013) and data points from other works. It should be noted that we show all LG dwarfs listed in Table 4 of Kirby et al. (2013). The presented fit, however, excludes the M31 dwarfs, since a different technique (coadded spectra) was used to estimate the metallicities and their uncertainties are larger when compared to the MW dwarfs. We note that our dwarf sample shows a wide range of different SNRs (see Figure 3). In order to gain robust estimates on the stellar populations high SNRs are needed (see Figure A.1. in Fahrion et al. 2019b). We are not able to reach high values for all galaxies but distinguish our results accordingly (see Figure 10, left vs. right).

On the left-hand plot in Figure 10 we show only quiescent dwarf galaxies and exclude cases with low SNR ($\lesssim 8$) spectra. On the right-hand plot, we show the full sample, including star forming galaxies (yellow) and galaxies with low SNR spectra (gray). As discussed in Section 2.5, we mask all emission lines in star forming galaxies to determine the stellar population properties age and metallicity. This leaves only the calcium triplet (CaT) for the estimation of these properties. Since the SNR in the remaining absorption spectrum is not high enough to make robust estimates, we treat these cases separately and note reduced reliability. For all but one of the galaxies with low SNRs (gray) the metallicity estimation is on the lower end of the possible val-

ues from the considered SSPs. For these cases we cannot derive meaningful results.

We see a systematic shift to lower metallicities in our sample compared with the LG dwarf galaxies. This shift is consistent with observations in other works: Fahrion et al. (2021) (Fornax & Virgo galaxies) and Fahrion et al. (2022) (nucleated dwarf LTGs) for this stellar mass range. As mentioned before (Section 1), however, this shift may be attributed to different strategies of measuring the metallicities between Kirby et al. (2013), this work and the other works cited in this study. Kirby et al. (2013) perform spectroscopy on individual RGB stars in order to obtain the metallicity, whereas we and other studies used for comparison (Fahrion et al. 2021, 2022; Müller et al. 2021; Chilingarian et al. 2019) measure the metallicity with full spectrum fitting. We are thus sensitive to the entire stellar population properties, whereas Kirby et al. (2013) present the mean metallicity over the RGB population in each galaxy. Another factor to consider is that the metallicities from Kirby et al. (2013) are based on the iron absorption lines (Fe I), while we use lines across the entire spectral range probed by MUSE (incl. H_β , H_α , the Mg Triplet, Fe I, Ca Triplet). The E-MILES ‘base’ models we are using assume that the integrated metallicity $[M/H]$ is equal to the iron metallicity $[Fe/H]$. This assumption, however, only holds true at high metallicities ($\gtrsim -1$ dex). Low metallicity stars – abundant in our dwarf galaxies – are alpha-enhanced which boosts $[M/H]$ compared to $[Fe/H]$. Considering this assumption, the $[Fe/H]$ as measured in Kirby et al. (2013) should be lower than the $[M/H]$ in our dwarf sample, which would make the discrepancy even stronger. We find that the SNR in our sample is too low to estimate $[Fe/H]$ directly via line index measurements (Vazdekis et al. 2010) or to determine $[Mg/Fe]$ as an additional fit parameter, which would help bridge the difference in the two measurement methods for the metallicity.

Boecker et al. (2020) use MUSE to compare age and metallicity measurements from individual stars and full spectrum fitting for the nuclear star cluster (NSC) M54. Interestingly, they find that the two methods show excellent agreement and note only a 3% difference in age and 0.2 dex in metallicity. The values for full spectrum fitting suggest older and more metal-poor stellar populations when compared to the integrated spectra from individual stars. The study finds a metal-poor and a metal-rich component in the NSC. The two methods are consistent on the low-metallicity component, while full spectrum fitting returns a higher metallicity estimate for the high-metallicity component. Similar to our study, the authors discuss alpha-abundances and find that, alpha-enhancement in metal-poor stars cannot explain the difference in these measurements since the exact opposite behavior would be expected in this context.

Below the mass-metallicity plots in Figure 10, we show the residual, i.e., the difference between the Kirby et al. (2013) relation and the data points. The gray dotted lines show the rms from Kirby et al. (2013). The systematic shift towards lower metallicities with the exception of three galaxies is even more apparent in this plot. A two-sample Kolmogorov–Smirnov (KS) test comparing the residual values for the LG dwarfs from Kirby et al. (2013) and the residuals from the clean sample (quiescent, medium to high SNR) in this work, reveals a p-value of $p = 0.002$. This indicates that the two samples show significant differences. While there is a significant scatter in other works (most notably Chilingarian et al. 2019), it is interesting that all but three galaxies in our sample show on average lower metallicity values than the MW dwarfs.

In order to test whether the insufficient SNR in some of our dwarf spectra could be a contributing factor in the discrepancy

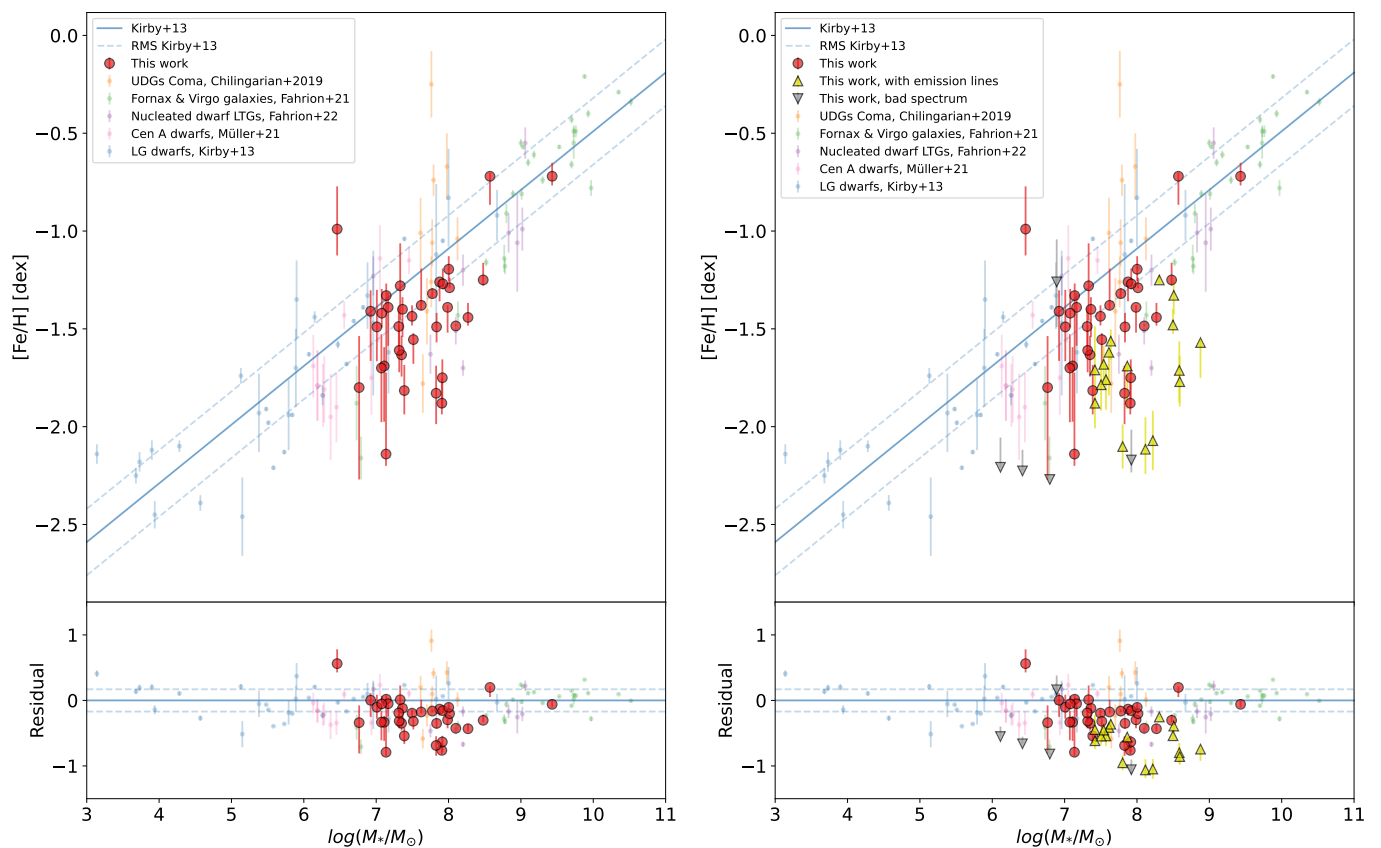


Fig. 10: Plotted is the universal stellar mass- metallicity relation from Kirby et al. (2013) as the blue solid line with its rms as the two blue dashed lines. On the x-axis we plot the logarithm of the stellar mass in units of solar mass. Left: we plot the data from this work (red circles) but exclude star forming and low SNR galaxies from this sample. Right: full sample from this work. Star forming galaxies are shown as yellow upward pointing triangles, while low SNR galaxies are gray downward pointing triangles. We compare our results with galaxies from other works: LG dwarfs (blue; Kirby et al. 2013), Cen A dwarfs (pink; Müller et al. 2021), galaxies in Fornax and Virgo (green; Fahrion et al. 2021), nucleated dwarf LTGs (purple; Fahrion et al. 2022) and UDGs in the Coma cluster (orange; Chilingarian et al. 2019). Bottom: residual plots, i.e. metallicity dwarf - metallicity fit. The blue dashed lines indicate the rms of the fit from Kirby et al. (2013). The LG dwarf metallicities from Kirby et al. (2013) are iron metallicities ([Fe/H]) while all other data points show total metallicities ([M/H]).

between Kirby et al. (2013) and this study, we deteriorate the quality of our highest SNR dwarf spectrum (MATLAS-553). To do this we first determine the best fit via pPXF and calculate the residuals between the best fit and the input galaxy spectrum at each wavelength. We then multiply the residuals with values from a Gaussian distribution with mean 0 and standard deviation σ and add the products back to the best fit at every wavelength. We then run pPXF on this newly generated spectrum and note the returned metallicity. In order to increase the statistical significance of this test, we create 100 realizations for a range of $\sigma \in [2,8]$ in steps of one. A higher value for σ leads to a higher degree of SNR deterioration compared to the original spectrum. In Figure 11 we present the results of this test, which shows the mean metallicity from 100 realizations as a function of σ . The error bars show the standard deviation of the MC metallicity distributions. As we would expect, the errors increase as the SNR becomes lower. If the low SNR in our sample would push the metallicity estimates towards lower values, we would expect a decreasing trend in this plot. Since we note no obvious behavior in that regard, we can rule out the SNR in our sample as a leading factor in the observed offset.

Considering the results from Boecker et al. (2020), the offset in the quiescent medium-to-high SNR dwarfs is fully mit-

igated by shifting the entire sample by 0.2 dex towards higher metallicities. A two-sample KS test yields a p-value of $p_{shift} = 0.8928$ after this shift, suggesting the two samples are consistent with following the same distribution. If we add the star forming galaxies to this test (low SNR galaxies excluded), however, the offset is still statistically significant with a KS p-value of $p_{shift\ all} = 0.0432$.

Another factor which could contribute to the offset in metallicities is the different environments in which the dwarf galaxies reside. We test this hypothesis by investigating the local density as described in Cappellari et al. (2011b) as a function of the residuals between the relation presented in Kirby et al. (2013) and the values from this study. The local density parameter

$$\rho_{10} = N_{gal} / \left(\frac{4}{3} \pi r_{10}^3 \right) \quad (2)$$

is defined as the 10 nearest massive galaxies N_{gal} of the assumed host galaxy divided by the sphere of radius r_{10} which encloses these 10 neighbors. In Habas et al. (2020) a correlation between this parameter and the morphology of the MATLAS dwarfs is found. We use the dwarf galaxies in our sample for which we could find a matching host in the ATLAS^{3D} survey

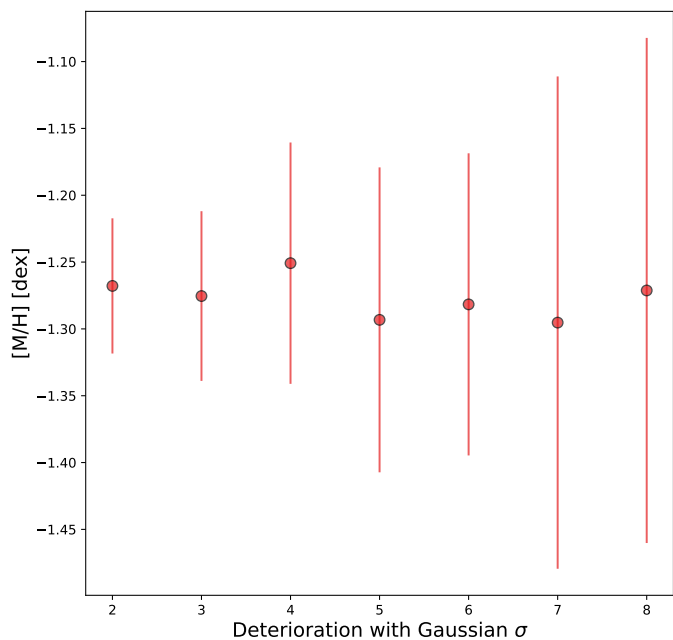


Fig. 11: Mean metallicity as a function of different degrees of spectrum deterioration for the highest SNR dwarf in the sample (MATLAS-553; SNR ~ 62). The error bars on the y-axis show the standard deviation of 100 MC realizations for every σ . The best fit value for the metallicity is -1.29 dex.

volume and compare its ρ_{10} measure with the metallicity offset from the MZR. We show the results of this test in Figure 12. Quiescent dwarfs are marked as red circles and star forming ones as yellow triangles. We note no apparent trend and can therefore not attribute the offset to the different density environments.

Finally, we test if the nucleus has any influence on the metallicity estimate and compare our results if we mask the nucleus or extract the spectra from the entire galaxy. We find very small differences between extracted metallicities with shifts in no particular direction. On average we find a difference of 0.002 dex towards lower metallicities with masked nuclei. For the dENs in our sample, the nucleus therefore does not contribute to the observed systematic offset.

In Figure 13 we show our results of the estimated age in Gyr versus the metallicity of our dwarf sample and compare with results from other works. It is important to note the large error bars for the age estimates, showing the difficulty of constraining this property with the quality type of spectra at hand. Overall we report an average old (6 to 14 Gyr) and metal poor (-1.9 to -1.3 dex) stellar population for most of these dwarf galaxies with a few outliers on the upper and lower end for the metallicity. We once again compare our sample with other works: galaxies in the Fornax and Virgo clusters are shown in green (Fahrion et al. 2021), nucleated dwarf LTGs in purple (Fahrion et al. 2022), the dwarf galaxies around Centaurus A in pink (Müller et al. 2021) and UDGs in the Coma cluster in orange (Chilingarian et al. 2019). Even though the measurement errors are rather large, we can see that our sample is concentrated in the lower right corner of Figure 13, comparable with the Cen A dwarfs (Müller et al. 2021). Cluster dwarfs and nucleated dwarf LTGs appear to span a larger range of ages in comparison.

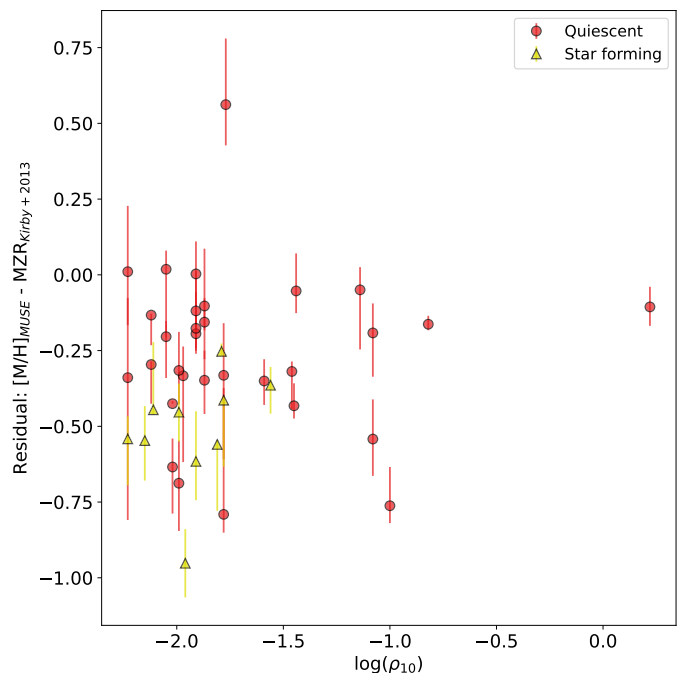


Fig. 12: Residuals between the metallicities for our dwarfs and the MZR from Kirby et al. (2013) as a function of the local density parameter ρ_{10} .

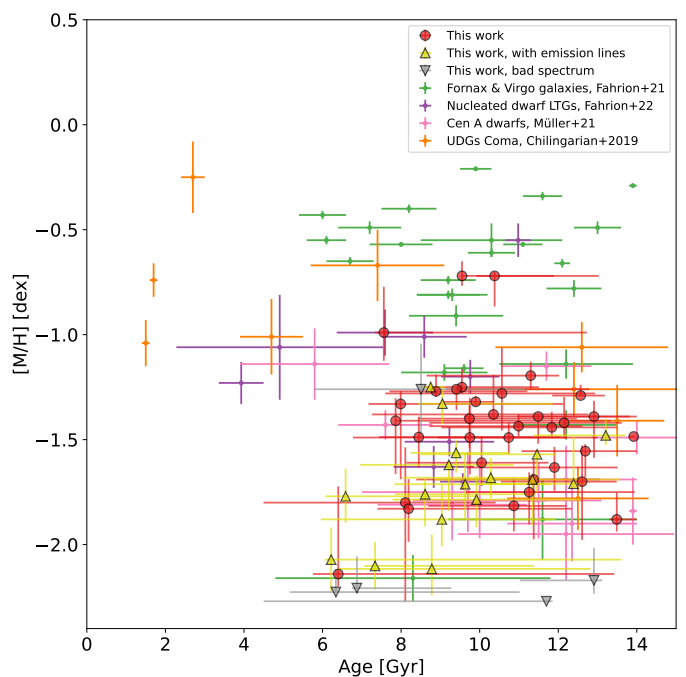


Fig. 13: Age vs. metallicity. The dwarf galaxies presented in this work are shown as red circles, yellow upwards pointing triangles (star forming) and gray downwards pointing triangles (low quality spectra). We compare with the results from other studies: galaxies in the Fornax and Virgo clusters (green; Fahrion et al. 2021), nucleated dwarf LTGs (purple; Fahrion et al. 2022), Cen A dwarfs (pink; Müller et al. 2021) and UDGs in the Coma cluster (orange; Chilingarian et al. 2019).

4. Conclusions

In this work, we analyze 56 dwarf galaxies based on MUSE spectroscopic observations. These galaxies are part of a large sample of dwarfs which have been previously identified in the MATLAS low-to-moderate density fields beyond the Local Volume. Through comparison with the overall photometric properties of the MATLAS dwarf sample, we find that our subsample observed with MUSE is representative of the dwarfs identified in MATLAS. Through full spectrum fitting with pPXF, we retrieve their line-of-sight velocity and stellar population properties age and metallicity. Our main results are the following:

1. The bulk of the 56 dwarfs, namely 42 (75%) show line-of-sight velocities which match the velocities of massive ATLAS^{3D} galaxies in the field, i.e., $\sim 1000 - 3000$ km/s. This number increases to 79% for dEs. Almost a third ($\sim 30%$) of the dwarf galaxies in the ATLAS^{3D} velocity range show star forming activity. Based on the minimal velocity difference ΔV between massive and dwarf galaxy, we determine the satellite membership of the dwarf galaxies in our sample. We update the previously assumed association in Figure 7 and conclude that our assumption (dwarfs are associated with the central, targeted ETG in each field) is correct in 57% of the cases for the presented sample.
2. We find that $\sim 18%$ (10) of the dwarfs in this sample are located further in the background, outside of the ATLAS^{3D} survey volume. Of these, 70% show emission lines, which is not unexpected in light of the semi-automatic identification approach for the MATLAS dwarfs (see Habas et al. 2020). There are no spectral lines apparent for 7% (4) of the dwarfs in this sample, thus we cannot extract any velocity information.
3. We demonstrate the viability the MUSE instrument for the study of low surface brightness dwarf galaxies in filler conditions and with a single observational block per galaxy. We determine the radius which optimizes the SNR of the extracted spectrum for each galaxy and relate it to the surface brightness in Figure 4. The distribution of surface brightnesses at the optimized radius illustrates that there are significant gains in probing to a depth of ~ 27 mag arcsec⁻² but diminishing returns in terms of SNR thereafter.
4. We find that the dwarfs presented in this work deviate from the universal stellar mass-metallicity relation shown in Kirby et al. (2013). The bulk of our sample is systematically offset towards lower metallicities, a property which, in this stellar mass range, can also be seen in dwarfs analyzed in other works. While the bulk of the sample with stellar masses in the range $10^{6.5} - 10^{8.5} M_*/M_\odot$ is more metal-poor than the LG dwarfs, only the two dwarfs with the highest stellar mass agree well with the universal mass-metallicity relation. We note that the star forming dwarfs in particular show a greater offset when compared to the quiescent ones. This could be due to the fact that only the CaT is left for this estimation, since all other lines show emissions and are therefore masked. The CaT may be insufficient to obtain a robust metallicity measurement.
5. The overall shift towards lower metallicities at a given stellar mass cannot be attributed to insufficient SNRs in our dwarf spectra nor to the different density environments the dwarf galaxies reside in.
6. We compare the age vs. metallicity of the dwarfs presented in this work with the results from other comparable studies in Figure 13. Although the error bars on the age are quite large, we can say that our sample is old (6-14 Gyr) and mostly

metal-poor (-1.3 - 1.9 dex), which is consistent with the Centaurus A satellites (Müller et al. 2021). Dwarfs located in clusters are more metal-rich and span a larger range of ages (Chilingarian et al. 2019; Fahrion et al. 2021).

Our results suggest that there may exist a systematic deviation from the LG stellar mass-metallicity relation. This deviation may, however, be due to the difference in methodologies for deriving metallicities. Kirby et al. (2013) base their results on individual RGB stars, while we and other works use full spectrum fitting. Boecker et al. (2020) find a measurement shift of 0.2 dex towards lower metallicities for full spectrum fitting when compared to the resolved stellar population analysis. By applying this shift towards higher metallicities, the offset is fully mitigated for the quiescent dwarfs but remains when also considering star forming dwarfs. This measurement difference is, however, based on the analysis of a single object and therefore does not hold statistical significance. In order to be able to paint a clearer picture on this matter, more methodology comparisons such as Boecker et al. (2020) are needed. In addition, more high quality spectra of dwarfs, in particular, in the mass domain between the dwarf and massive galaxy regime will help clarify if the offset only occurs for dwarfs below a certain stellar mass threshold, since our highest mass galaxies as well as high mass galaxies from other works are consistent with the MZR. From our results it is plausible that full spectrum fitting of dwarf galaxies may lead to a steeper slope for the MZR or even a non-linear relation.

Acknowledgements. We thank the referee for the constructive report, which helped to clarify and improve the manuscript. N.H. and O.M. are grateful to the Swiss National Science Foundation for financial support under the grant number PZ00P2_202104. M.P. is supported by the Academy of Finland grant n:o 347089. S.L. acknowledges the support from the Sejong Science Fellowship Program by the National Research Foundation of Korea (NRF) grand funded by the Korea government (MSIT) (No. NRF-2021R1C1C2006790). N.H. and O.M. thank Guissepina Battaglia for pointing out the work by Boecker et al. (2020). We thank the International Space Science Institute (ISSI) in Bern (Switzerland) for hosting our international team for a workshop on "Space Observations of Dwarf Galaxies from Deep Large Scale Surveys: The MATLAS Experience".

References

- Andrews, B. H. & Martini, P. 2013, *The Astrophysical Journal*, 765, 140
- Bacon, R., Accardo, M., Adjali, L., et al. 2010, in *Ground-based and Airborne Instrumentation for Astronomy III*, Vol. 7735, SPIE, 131–139
- Bacon, R., Accardo, M., Adjali, L., et al. 2012, *The Messenger*, 147, 4
- Bell, E. F., Slater, C. T., & Martin, N. F. 2011, *ApJ*, 742, L15
- Bennet, P., Sand, D., Crnojević, D., et al. 2019, *The Astrophysical Journal*, 885, 153
- Bennet, P., Sand, D., Crnojević, D., et al. 2017, *The Astrophysical Journal*, 850, 109
- Bennet, P., Sand, D. J., Crnojević, D., et al. 2020, *ApJ*, 893, L9
- Bennet, P., Sand, D. J., Crnojević, D., et al. 2017, *ApJ*, 850, 109
- Bertin, E. & Arnouts, S. 1996, *Astronomy and Astrophysics Supplement Series*, 117, 393
- Bílek, M., Duc, P.-A., Cuillandre, J.-C., et al. 2020, *MNRAS*, 498, 2138
- Binggeli, B. & Jerjen, H. 1997, in *Galaxy Scaling Relations: Origins, Evolution and Applications: Proceedings of the ESO Workshop Held at Garching, Germany, 18–20 November 1996*, Springer, 103–112
- Binggeli, B., Tarenghi, M., & Sandage, A. 1990, *A&A*, 228, 42
- Boecker, A., Alfaro-Cuello, M., Neumayer, N., Martín-Navarro, I., & Leaman, R. 2020, *ApJ*, 896, 13
- Brook, C., Stinson, G., Gibson, B. K., et al. 2014, *Monthly Notices of the Royal Astronomical Society*, 443, 3809
- Brooks, A. M., Governato, F., Booth, C., et al. 2007, *The Astrophysical Journal*, 655, L17
- Bullock, J. S. & Boylan-Kolchin, M. 2017, *Annual Review of Astronomy and Astrophysics*, 55
- Buonanno, R., Corsi, C., Fusi Pecci, F., Hardy, E., & Zinn, R. 1985, *Astronomy and Astrophysics (ISSN 0004-6361)*, vol. 152, no. 1, Nov. 1985, p. 65-84. NSERC-supported research., 152, 65

- Cappellari, M. 2017, *MNRAS*, 466, 798
- Cappellari, M., Bacon, R., Bureau, M., et al. 2006, *Monthly Notices of the Royal Astronomical Society*, 366, 1126
- Cappellari, M. & Emsellem, E. 2004, *PASP*, 116, 138
- Cappellari, M., Emsellem, E., Krajnović, D., et al. 2011, *Monthly Notices of the Royal Astronomical Society*, 413, 813
- Cappellari, M., Emsellem, E., Krajnović, D., et al. 2011a, *MNRAS*, 413, 813
- Cappellari, M., Emsellem, E., Krajnović, D., et al. 2011b, *MNRAS*, 416, 1680
- Carlsten, S. G., Beaton, R. L., Greco, J. P., & Greene, J. E. 2019, *ApJ*, 878, L16
- Carlsten, S. G., Greene, J. E., Beaton, R. L., Danieli, S., & Greco, J. P. 2022, *ApJ*, 933, 47
- Chiboucas, K., Jacobs, B. A., Tully, R. B., & Karachentsev, I. D. 2013, *AJ*, 146, 126
- Chilingarian, I. V., Afanasiev, A. V., Grishin, K. A., Fabricant, D., & Moran, S. 2019, *ApJ*, 884, 79
- Chiosi, C., D’Onofrio, M., Merlin, E., Piovan, L., & Marziani, P. 2020, *Astronomy & Astrophysics*, 643, A136
- Cohen, Y., van Dokkum, P., Danieli, S., et al. 2018, *ApJ*, 868, 96
- Courteau, S., Dutton, A. A., van den Bosch, F. C., et al. 2007, *Scaling Relations of Spiral Galaxies*, 671 (1): 203–225
- Cowie, L. L., Songaila, A., Hu, E. M., & Cohen, J. 1996, arXiv preprint astro-ph/9606079
- Crnojević, D., Sand, D. J., Bennet, P., et al. 2019, *ApJ*, 872, 80
- Danieli, S., van Dokkum, P., Merritt, A., et al. 2017, *ApJ*, 837, 136
- Danieli, S., van Dokkum, P., Trujillo-Gomez, S., et al. 2022, *ApJ*, 927, L28
- Davis, A. B., Nierenberg, A. M., Peter, A. H. G., et al. 2021, *MNRAS*, 500, 3854
- Djorgovski, S. & Davis, M. 1987, *ApJ*, 313, 59
- Dressler, A., Lynden-Bell, D., Burstein, D., et al. 1987, *ApJ*, 313, 42
- Drlica-Wagner, A., Bechtol, K., Mau, S., et al. 2020, *ApJ*, 893, 47
- Drlica-Wagner, A., Carlin, J. L., Nidever, D. L., et al. 2021, *ApJS*, 256, 2
- Duc, P.-A., Cuillandre, J.-C., Karabal, E., et al. 2015, *Monthly Notices of the Royal Astronomical Society*, 446, 120
- D’Onofrio, M., Marziani, P., & Chiosi, C. 2021, *Frontiers in Astronomy and Space Sciences*, 157
- Eigenthaler, P., Puzia, T. H., Taylor, M. A., et al. 2018, *The Astrophysical Journal*, 855, 142
- Emsellem, E., van der Burg, R. F. J., Fensch, J., et al. 2019, *A&A*, 625, A76
- Erb, D. K., Steidel, C. C., Shapley, A. E., et al. 2006, *The Astrophysical Journal*, 646, 107
- Faber, S. & Jackson, R. E. 1976, *The Astrophysical Journal*, 204, 668
- Fahrion, K., Bulichi, T.-E., Hilker, M., et al. 2022, *A&A*, 667, A101
- Fahrion, K., Georgiev, I., Hilker, M., et al. 2019a, *A&A*, 625, A50
- Fahrion, K., Lyubenova, M., van de Ven, G., et al. 2021, *A&A*, 650, A137
- Fahrion, K., Lyubenova, M., van de Ven, G., et al. 2019b, *A&A*, 628, A92
- Fahrion, K., Müller, O., Rejkuba, M., et al. 2020, *Astronomy & Astrophysics*, 634, A53
- Fensch, J., van der Burg, R. F. J., Jeřábková, T., et al. 2019, *A&A*, 625, A77
- Ferguson, H., Sandage, A., Hollenbach, D., & AJ, T. H. 1990
- Ferguson, H. C. & Binggeli, B. 1994, *A&A Rev.*, 6, 67
- Ferguson, H. C. & Sandage, A. 1989, *The Astrophysical Journal*, 346, L53
- Ferrarese, L., Cote, P., Cuillandre, J.-C., et al. 2012, *The Astrophysical Journal Supplement Series*, 200, 4
- Fitzpatrick, P. J. & Graves, G. J. 2015, *Monthly Notices of the Royal Astronomical Society*, 447, 1383
- Font, A. S., Benson, A. J., Bower, R. G., et al. 2011, *MNRAS*, 417, 1260
- Freedman, W. L. 2021, *The Astrophysical Journal*, 919, 16
- Frenk, C. S. & White, S. D. M. 2012, *Annalen der Physik*, 524, 507
- Gallazzi, A., Charlot, S., Brinchmann, J., & White, S. D. M. 2006, *MNRAS*, 370, 1106
- Gallazzi, A., Charlot, S., Brinchmann, J., White, S. D. M., & Tremonti, C. A. 2005, *MNRAS*, 362, 41
- Garnett, D. R. 2002, *The Astrophysical Journal*, 581, 1019
- Geha, M., Wechsler, R. H., Mao, Y.-Y., et al. 2017, *ApJ*, 847, 4
- González Delgado, R. M., Cid Fernandes, R., García-Benito, R., et al. 2014, *ApJ*, 791, L16
- Greco, J. P., Greene, J. E., Strauss, M. A., et al. 2018, *ApJ*, 857, 104
- Guérou, A., Krajnović, D., Epinat, B., et al. 2017, *A&A*, 608, A5
- Habas, R., Marleau, F. R., Duc, P.-A., et al. 2020, *Monthly Notices of the Royal Astronomical Society*, 491, 1901
- Heesters, N., Habas, R., Marleau, F. R., et al. 2021, *A&A*, 654, A161
- Hou, J., Yu, Q., & Lu, Y. 2014, *ApJ*, 791, 8
- Ibata, R., Martin, N. F., Irwin, M., et al. 2007, *ApJ*, 671, 1591
- Ibata, R. A., Lewis, G. F., Conn, A. R., et al. 2013, *Nature*, 493, 62
- Ibata, R. A., Lewis, G. F., McConnachie, A. W., et al. 2014, *ApJ*, 780, 128
- Irwin, J. A., Hoffman, G. L., Spekkens, K., et al. 2009, *ApJ*, 692, 1447
- Kewley, L. J. & Ellison, S. L. 2008, *The Astrophysical Journal*, 681, 1183
- Kim, E., Kim, M., Hwang, N., et al. 2011, *MNRAS*, 412, 1881
- Kim, S. Y., Peter, A. H. G., & Hargis, J. R. 2018, *Phys. Rev. Lett.*, 121, 211302
- Kirby, E. N., Cohen, J. G., Guhathakurta, P., et al. 2013, *The Astrophysical Journal*, 779, 102
- Koposov, S., Belokurov, V., Evans, N. W., et al. 2008, *ApJ*, 686, 279
- Köppen, J., Weidner, C., & Kroupa, P. 2007, *Monthly Notices of the Royal Astronomical Society*, 375, 673
- Kormendy, J. 1977, *ApJ*, 218, 333
- Kroupa, P. 2001, *MNRAS*, 322, 231
- Kunkel, W. E. & Demers, S. 1976, in *The Galaxy and the Local Group*, Vol. 182, 241
- Kuntschner, H., Lucey, J. R., Smith, R. J., Hudson, M. J., & Davies, R. L. 2001, *Monthly Notices of the Royal Astronomical Society*, 323, 615
- La Barbera, F., Busarello, G., Merluzzi, P., et al. 2008, *The Astrophysical Journal*, 689, 913
- La Marca, A., Peletier, R., Iodice, E., et al. 2022, *A&A*, 659, A92
- Lee, H., Skillman, E. D., Cannon, J. M., et al. 2006, *ApJ*, 647, 970
- Lequeux, J., Peimbert, M., Rayo, J., Serrano, A., & Torres-Peimbert, S. 1979, *Astronomy and Astrophysics*, vol. 80, no. 2, Dec. 1979, p. 155–166., 80, 155
- Li, Y.-S., De Lucia, G., & Helmi, A. 2010, *MNRAS*, 401, 2036
- Lian, J., Thomas, D., & Maraston, C. 2018, *Monthly Notices of the Royal Astronomical Society*, 481, 4000
- Lu, Y., Benson, A., Wetzel, A., et al. 2017, *ApJ*, 846, 66
- Lu, Y., Wechsler, R. H., Somerville, R. S., et al. 2014, *ApJ*, 795, 123
- Lupton, R. 2005, *Transformations between SDSS magnitudes and other systems*
- Lynden-Bell, D. 1976, *Monthly Notices of the Royal Astronomical Society*, 174, 695
- Ma, X., Hopkins, P. F., Faucher-Giguère, C.-A., et al. 2016, *Monthly Notices of the Royal Astronomical Society*, 456, 2140
- Magorrian, J., Tremaine, S., Richstone, D., et al. 1998, *AJ*, 115, 2285
- Maiolino, R. & Mannucci, F. 2019, *A&A Rev.*, 27, 3
- Mannucci, F., Cresci, G., Maiolino, R., Marconi, A., & Gnerucci, A. 2010, *MNRAS*, 408, 2115
- Mao, Y.-Y., Geha, M., Wechsler, R. H., et al. 2021, *ApJ*, 907, 85
- Marleau, F. R., Habas, R., Poulain, M., et al. 2021, *A&A*, 654, A105
- Martin, N. F., Ibata, R. A., Irwin, M. J., et al. 2006, *MNRAS*, 371, 1983
- Martin, N. F., Ibata, R. A., Lewis, G. F., et al. 2016, *ApJ*, 833, 167
- Mateo, M. L. 1998, *ARA&A*, 36, 435
- McClure, R. D. & van den Bergh, S. 1968, *AJ*, 73, 1008
- McConnachie, A. W. 2012, *AJ*, 144, 4
- McConnachie, A. W., Ibata, R., Martin, N., et al. 2018, *ApJ*, 868, 55
- McConnachie, A. W., Irwin, M. J., Ibata, R. A., et al. 2009, *Nature*, 461, 66
- Mollá, M., Cavichia, O., Gavilán, M., & Gibson, B. K. 2015, *Monthly Notices of the Royal Astronomical Society*, 451, 3693
- Mouhcine, M., Kriwattanawong, W., & James, P. 2011, *Monthly Notices of the Royal Astronomical Society*, 412, 1295
- Mould, J. R., Kristian, J., & Da Costa, G. S. 1983, *ApJ*, 270, 471
- Müller, O., Durrell, P. R., Marleau, F. R., et al. 2021, *ApJ*, 923, 9
- Müller, O., Fahrion, K., Rejkuba, M., et al. 2021, *Astronomy & Astrophysics*, 645, A92
- Müller, O., Fahrion, K., Rejkuba, M., et al. 2021, *A&A*, 645, A92
- Müller, O. & Jerjen, H. 2020, *A&A*, 644, A91
- Müller, O., Jerjen, H., Pawlowski, M. S., & Binggeli, B. 2016, *Astronomy & Astrophysics*, 595, A119
- Müller, O., Marleau, F. R., Duc, P.-A., et al. 2020, *A&A*, 640, A106
- Müller, O., Marleau, F. R., Duc, P.-A., et al. 2020, *Astronomy & Astrophysics*, 640, A106
- Müller, O., Pawlowski, M. S., Jerjen, H., & Lelli, F. 2018, *Science*, 359, 534
- Müller, O., Pawlowski, M. S., Lelli, F., et al. 2021, *Astronomy & Astrophysics*, 645, L5
- Müller, O., Rejkuba, M., Pawlowski, M. S., et al. 2019, *Astronomy & Astrophysics*, 629, A18
- Munshi, F., Brooks, A. M., Applebaum, E., et al. 2021, *ApJ*, 923, 35
- Mutlu-Pakdil, B., Sand, D. J., Crnojević, D., et al. 2022, *ApJ*, 926, 77
- Nadler, E. O., Mao, Y.-Y., Green, G. M., & Wechsler, R. H. 2019, *ApJ*, 873, 34
- Panther, B., Jimenez, R., Heavens, A. F., & Charlot, S. 2008, *MNRAS*, 391, 1117
- Park, H. S., Moon, D.-S., Zaritsky, D., et al. 2017, *ApJ*, 848, 19
- Pasquali, A., Gallazzi, A., Fontanot, F., et al. 2010, *Monthly Notices of the Royal Astronomical Society*, 407, 937
- Pawlowski, M., Pflamm-Altenburg, J., & Kroupa, P. 2012, *Monthly Notices of the Royal Astronomical Society*, 423, 1109
- Peng, C. Y., Ho, L. C., Impey, C. D., & Rix, H.-W. 2002, *The Astronomical Journal*, 124, 266
- Peng, C. Y., Ho, L. C., Impey, C. D., & Rix, H.-W. 2010, *The Astronomical Journal*, 139, 2097
- Peng, Y., Maiolino, R., & Cochrane, R. 2015, *Nature*, 521, 192
- Poulain, M., Marleau, F. R., Habas, R., et al. 2021, *Monthly Notices of the Royal Astronomical Society*
- Poulain, M., Marleau, F. R., Habas, R., et al. 2022, *A&A*, 659, A14
- Prole, D. J., van der Burg, R. F. J., Hilker, M., & Spitler, L. R. 2021, *MNRAS*, 500, 2049
- Sánchez-Blázquez, P., Gorgas, J., Cardiel, N., & González, J. 2006, *Astronomy & Astrophysics*, 457, 809
- Sandage, A. 1972, *ApJ*, 176, 21

- Sawala, T., Cautun, M., Frenk, C., et al. 2022, *Nature Astronomy* [arXiv:2205.02860]
- Sawala, T., Scannapieco, C., & White, S. 2012, *Monthly Notices of the Royal Astronomical Society*, 420, 1714
- Sheth, R. K., Jimenez, R., Panter, B., & Heavens, A. F. 2006, *The Astrophysical Journal*, 650, L25
- Simon, J. D. 2019, *ARA&A*, 57, 375
- Soto, K. T., Lilly, S. J., Bacon, R., Richard, J., & Conseil, S. 2016, *MNRAS*, 458, 3210
- Steyrleithner, P., Hensler, G., & Boselli, A. 2020, *Monthly Notices of the Royal Astronomical Society*, 494, 1114
- Stierwalt, S., Haynes, M. P., Giovanelli, R., et al. 2009, *AJ*, 138, 338
- Su, A. H., Salo, H., Janz, J., et al. 2021, *A&A*, 647, A100
- Sybiliska, A., Lisker, T., Kuntschner, H., et al. 2017, *Monthly Notices of the Royal Astronomical Society*, 470, 815
- Tammann, G. 1994, in *European Southern Observatory Conference and Workshop Proceedings*, Vol. 49, 3
- Tanoglidis, D., Drlaca-Wagner, A., Wei, K., et al. 2021, *ApJS*, 252, 18
- Tassis, K., Kravtsov, A. V., & Gnedin, N. Y. 2008, *The Astrophysical Journal*, 672, 888
- Teeninga, P., Moschini, U., Trager, S. C., & Wilkinson, M. H. 2015, in *International Symposium on Mathematical Morphology and Its Applications to Signal and Image Processing*, Springer, 157–168
- Thomas, D., Maraston, C., & Bender, R. 2005, in *Multiwavelength Mapping of Galaxy Formation and Evolution: Proceedings of the ESO Workshop Held at Venice, Italy, 13-16 October 2003*, Springer, 296–301
- Thomas, D., Maraston, C., Schawinski, K., Sarzi, M., & Silk, J. 2010, *Monthly Notices of the Royal Astronomical Society*, 404, 1775
- Tolstoy, E., Hill, V., & Tosi, M. 2009, *Annual Review of Astronomy and Astrophysics*, 47, 371
- Trager, S., Faber, S., Worthey, G., & González, J. J. 2000, *The Astronomical Journal*, 120, 165
- Tremonti, C. A., Heckman, T. M., Kauffmann, G., et al. 2004, *The Astrophysical Journal*, 613, 898
- Trussler, J., Maiolino, R., Maraston, C., et al. 2020, *Monthly Notices of the Royal Astronomical Society*, 491, 5406
- Tully, R. B. & Fisher, J. R. 1977, *Astronomy and Astrophysics*, vol. 54, no. 3, Feb. 1977, p. 661-673., 54, 661
- Vaduvescu, O., McCall, M. L., & Richer, M. G. 2007, *The Astronomical Journal*, 134, 604
- Vazdekis, A., Koleva, M., Ricciardelli, E., Röck, B., & Falcón-Barroso, J. 2016, *Monthly Notices of the Royal Astronomical Society*, 463, 3409
- Vazdekis, A., Sánchez-Blázquez, P., Falcón-Barroso, J., et al. 2010, *MNRAS*, 404, 1639
- Venhola, A., Peletier, R., Laurikainen, E., et al. 2019, *Astronomy & astrophysics*, 625, A143
- Vincenzo, F., Matteucci, F., Belfiore, F., & Maiolino, R. 2016, *Monthly Notices of the Royal Astronomical Society*, 455, 4183
- Xia, M. & Yu, Q. 2019a, *The Astrophysical Journal*, 874, 105
- Xia, M. & Yu, Q. 2019b, *The Astrophysical Journal*, 880, 5
- Zahid, H., Bresolin, F., Kewley, L., Coil, A. L., & Davé, R. 2012, *The Astrophysical Journal*, 750, 120
- Zaritsky, D., Donnerstein, R., Dey, A., et al. 2019, *ApJS*, 240, 1
- Zhang, H.-X., Puzia, T. H., Peng, E. W., et al. 2018, *The Astrophysical Journal*, 858, 37

Appendix A: Supplementary materials

Appendix A.1: Dwarf galaxy cutouts

In Figure [A.1](#) we present cutouts of the 56 dwarf galaxies studied in this work. We collapse the MUSE datacubes along the wavelength axis by taking the median of each spaxel to produce the images.

Appendix A.2: Error estimation

In this section we show the results of the error estimation via MC simulations. The signs of the residuals between galaxy spectrum and best fit are flipped randomly and refitted with pPXF. This is done in 400 realizations per galaxy which results in distributions for the extracted properties velocity, age and metallicity. In some cases the best fit value lies outside of the 1σ confidence interval from the MC realizations (see Figure [5](#)). In Figure [A.2](#) we show the residual of the best fit minus the mean/median of the MC realizations and indicate by color whether or not the best fit value lies within (green) or outside (red) the 1σ bounds of the MC simulations.

Appendix A.3: Data table

We summarize the properties of the 56 dwarfs studied in this work in Table [A.1](#). We obtained the values from [Habas et al. \(2020\)](#), [Poulain et al. \(2021\)](#) and this work.

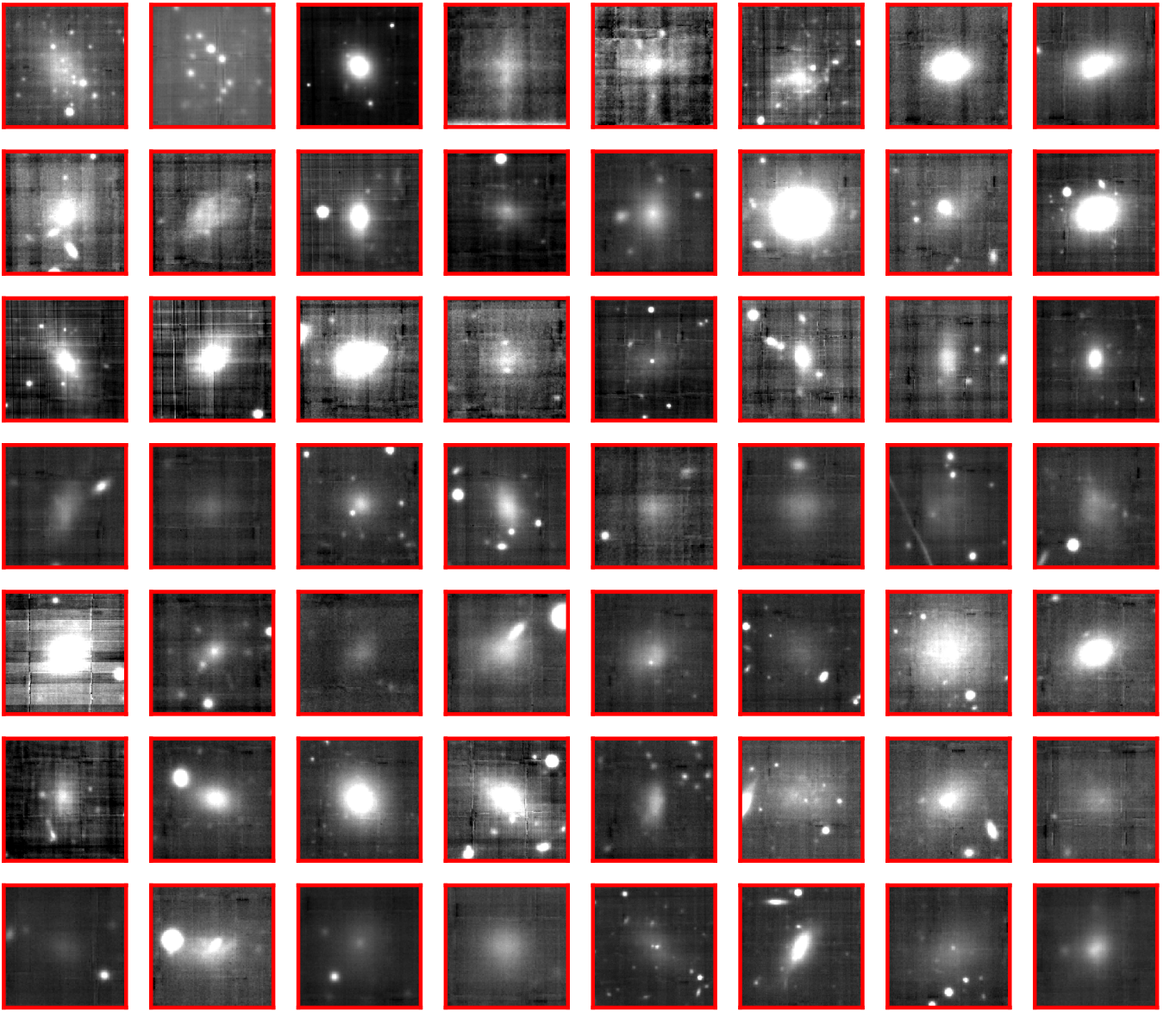


Fig. A.1: Cutouts of all dwarf galaxies produced by collapsing the MUSE data cubes along the wavelength axis, resulting in 2D images. The size of the cutouts are chosen to be the diameter of the dwarf's visual appearance in the MUSE image plus a margin of 2 arcsec.

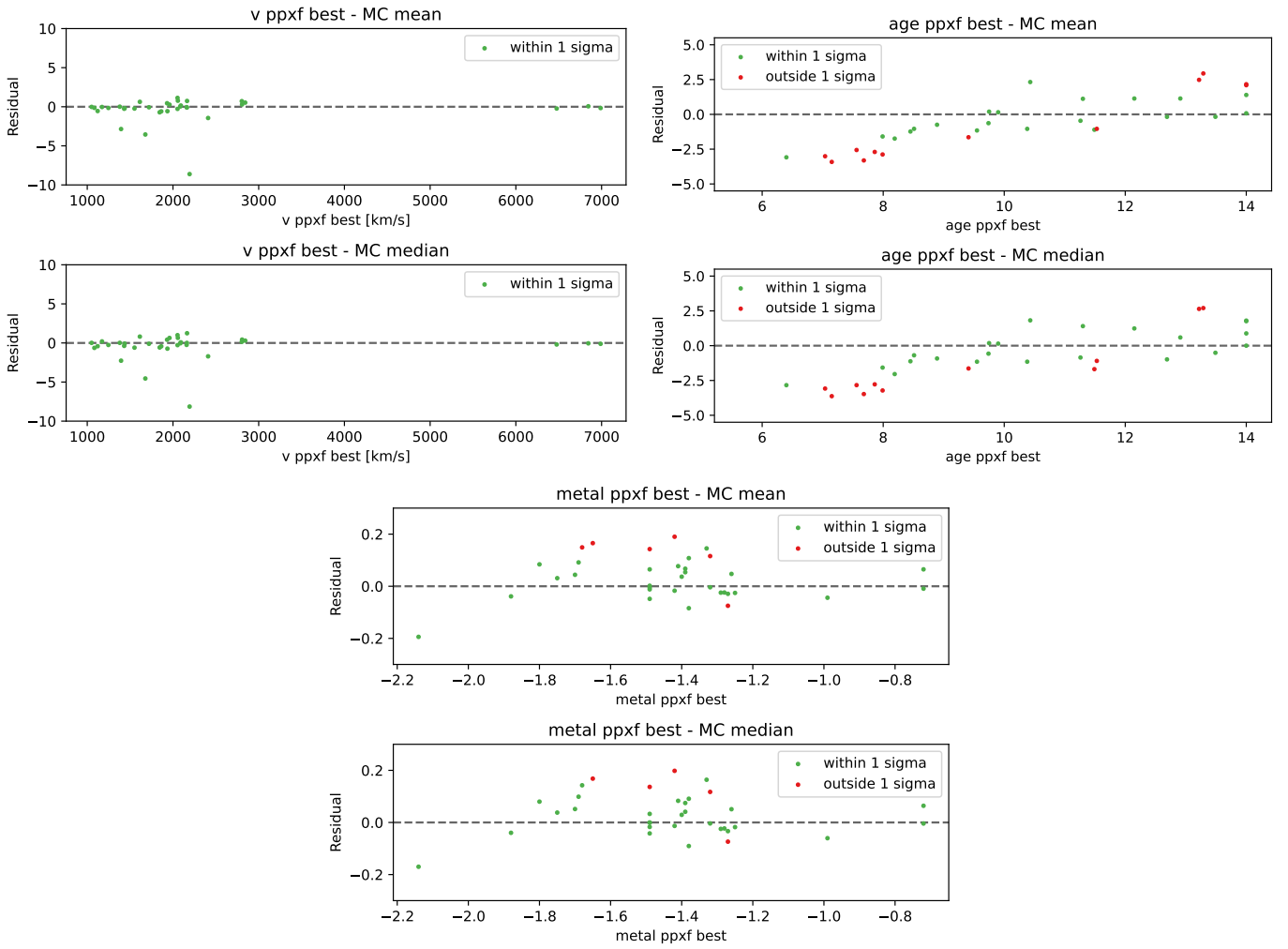


Fig. A.2: Residual plots of the pPXF best fit values subtracted by the mean and median of the MC realizations for the parameters: recessional velocity (v ; top left), age (top right), metallicity (bottom center). Green dots indicate that the best fit value resides inside the 1σ bounds of the MC realizations, red means the value is outside of these bounds.

Table A.1: Properties of the dwarf galaxies studied in this work.

ID	Morph	RA	Dec	Host	D	M_g	R_{eff}	Em	Bkg	V	Age	[M/H]	ML	SNR	Q
(1)	(2)	[deg]	[deg]	(5)	[Mpc]	[mag]	[$''$]	(9)	(10)	[km/s]	[Gyr]	[dex]	(14)	(15)	(16)
1297	dE	184.7614	5.0981	NGC4255	31.0	17.9	13.1	0	0	1931.3 $^{+3.9}_{-5.0}$	11.8 $^{+1.7}_{-2.8}$	-1.44 $^{+0.07}_{-0.04}$	2.2 $^{+0.0}_{-0.6}$	24.0	1
2019	dE	226.3340	1.8127	NGC5846	21.0	17.8	17.2	0	0	2158.8 $^{+5.2}_{-5.1}$	13.5 $^{+0.5}_{-0.2}$	-1.88 $^{+0.13}_{-0.06}$	2.1 $^{+0.1}_{-0.0}$	24.3	1
10	dEN	18.7949	-1.4718	NGC0448	30.0	17.3	4.4	1	0	1852.5 $^{+1.4}_{-1.9}$	8.8 $^{+0.4}_{-0.2}$	-1.25 $^{+0.03}_{-0.01}$	1.6 $^{+0.1}_{-0.0}$	61.9	1
35	dE	20.4945	3.9712	NGC0474	31.0	19.9	5.1	0	0	2193.8 $^{+27.5}_{-9.7}$	6.4 $^{+7.0}_{-0.6}$	-2.14 $^{+0.42}_{-0.06}$	1.2 $^{+0.8}_{-0.1}$	9.3	1
205	dI	42.3268	-1.5714		37.0	18.9	6.5	0		2603.7 $^{+12.6}_{-17.0}$	12.9 $^{+0.2}_{-1.9}$	-2.17 $^{+0.16}_{-0.06}$	2.1 $^{+0.0}_{-0.3}$	13.4	0
223	dI	43.1790	-1.3266		60.0	18.0	9.8	1	1	4167.3 $^{+9.8}_{-11.6}$	9.6 $^{+2.2}_{-1.8}$	-1.71 $^{+0.15}_{-0.16}$	1.7 $^{+0.2}_{-0.3}$	19.0	1
300	dE	49.9520	-2.3088		93.0	19.4	3.1	0	1	6476.1 $^{+4.7}_{-4.5}$	9.5 $^{+2.0}_{-0.9}$	-1.25 $^{+0.09}_{-0.03}$	1.6 $^{+0.3}_{-0.0}$	21.1	1
303	dE	50.0618	-1.7127	NGC1289	38.0	19.0	5.6	0	0	2806.1 $^{+3.3}_{-3.6}$	9.4 $^{+3.4}_{-0.3}$	-1.26 $^{+0.0}_{-0.1}$	1.8 $^{+0.4}_{-0.0}$	25.0	1
290	dE	49.5108	-1.6533	NGC1289	38.0	18.8	8.2	0	0	2842.5 $^{+8.1}_{-9.4}$	11.5 $^{+2.5}_{-0.5}$	-1.39 $^{+0.01}_{-0.13}$	1.9 $^{+0.3}_{-0.1}$	15.9	1
313	dI	71.6313	-5.2406		67.0	19.1	6.4	1	1	4709.9 $^{+6.5}_{-21.2}$	8.8 $^{+4.0}_{-2.4}$	-2.12 $^{+0.16}_{-0.13}$	1.2 $^{+0.7}_{-0.1}$	13.2	1
445	dE	134.2161	-3.2605	NGC2699	26.0	18.9	4.1	0	0	2053.2 $^{+3.4}_{-2.7}$	11.0 $^{+1.6}_{-2.3}$	-1.44 $^{+0.06}_{-0.05}$	1.5 $^{+0.6}_{-0.2}$	32.4	1
443	dE	134.1938	-3.2526	NGC2699	26.0	19.0	4.9	0	0	1959.5 $^{+5.3}_{-5.9}$	10.4 $^{+2.4}_{-3.1}$	-1.38 $^{+0.19}_{-0.02}$	2.2 $^{+0.0}_{-0.7}$	13.8	1
444	dEN	134.2092	-2.9154	NGC2699	26.0	19.4	4.9	0	0	2091.8 $^{+4.7}_{-5.1}$	9.7 $^{+2.7}_{-1.3}$	-1.4 $^{+0.06}_{-0.14}$	1.7 $^{+0.3}_{-0.1}$	21.3	1
553	dEN	145.4222	-3.7319	NGC2974	21.0	17.5	6.7	0	0	1719.9 $^{+1.7}_{-1.6}$	12.6 $^{+0.6}_{-0.7}$	-1.29 $^{+0.05}_{-0.0}$	2.0 $^{+0.3}_{-0.1}$	63.0	1
574	dE	146.1150	-3.3048	NGC2974	21.0	19.5	7.2	0	0	1935.1 $^{+9.1}_{-7.8}$	8.0 $^{+4.1}_{-0.8}$	-1.33 $^{+0.06}_{-0.36}$	1.5 $^{+0.5}_{-0.1}$	12.8	1
1476	dEN	191.5301	-3.2690	NGC4691	16.0	17.4	6.6	0	0	1050.7 $^{+1.4}_{-1.5}$	9.9 $^{+0.5}_{-0.9}$	-1.32 $^{+0.03}_{-0.02}$	1.8 $^{+0.1}_{-0.1}$	55.0	1
1486	dEN	191.7061	-2.5005		64.0	17.6	9.1	1	1	4474.8 $^{+0.5}_{-8.8}$	11.5 $^{+0.5}_{-3.0}$	-1.57 $^{+0.01}_{-0.18}$	1.9 $^{+0.0}_{-0.3}$	34.1	1
324	dE	72.6729	-3.8295		65.0	18.7	4.1	1	1	4563.4 $^{+1.7}_{-9.4}$	13.2 $^{+0.5}_{-1.8}$	-1.48 $^{+0.08}_{-0.05}$	2.1 $^{+0.1}_{-0.3}$	24.4	1
323	dE	72.6134	-3.6137		64.0	18.5	4.9	1	1	4492.5 $^{+5.3}_{-5.2}$	9.0 $^{+2.8}_{-0.6}$	-1.33 $^{+0.08}_{-0.1}$	1.7 $^{+0.3}_{-0.1}$	22.9	1
321	dE	72.4610	-3.5938		14.0	19.9	4.8	0		963.0 $^{+16.2}_{-24.3}$	6.3 $^{+4.7}_{-1.2}$	-2.23 $^{+0.11}_{-0.0}$	1.2 $^{+0.5}_{-0.2}$	8.4	0
1408	dEN	190.2965	-5.0977	NGC4546	14.0	18.8	8.5	0	0	1083.1 $^{+7.0}_{-7.5}$	12.9 $^{+0.9}_{-3.3}$	-1.39 $^{+0.08}_{-0.2}$	2.1 $^{+0.2}_{-0.4}$	14.5	1
15	dE	18.9577	-1.3915		14.0	19.8	4.3	0		1015.0 $^{+81.4}_{-67.2}$	11.7 $^{+0.2}_{-7.2}$	-2.27 $^{+0.0}_{-0.0}$	2.1 $^{+0.0}_{-0.9}$	13.3	0
29	dE	20.1466	3.1456	NGC0474	31.0	19.2	7.6	1	0	2153.4 $^{+10.2}_{-10.6}$	9.2 $^{+1.6}_{-2.3}$	-1.62 $^{+0.01}_{-0.22}$	1.9 $^{+0.2}_{-0.7}$	13.2	1
222	dE	43.1665	-1.1599		98.0	19.6	4.0	0	1	6845.4 $^{+3.2}_{-3.5}$	10.4 $^{+2.6}_{-0.5}$	-0.72 $^{+0.02}_{-0.15}$	2.3 $^{+0.4}_{-0.1}$	23.5	1
273	dE	48.9098	-2.9508	NGC1266	30.0	19.6	6.3	1	0	2522.1 $^{+5.6}_{-16.1}$	12.4 $^{+0.3}_{-2.5}$	-1.71 $^{+0.22}_{-0.02}$	2.0 $^{+0.0}_{-0.3}$	15.8	1
269	dE	48.6046	-2.9236	NGC1253	16.0	20.4	4.9	0	0	1613.6 $^{+11.9}_{-12.7}$	7.6 $^{+5.2}_{-0.2}$	-0.99 $^{+0.22}_{-0.13}$	1.6 $^{+0.9}_{-0.0}$	8.7	1
448	dE	134.2757	-3.3425	NGC2699	26.0	20.4	3.2	0	0	2053.2 $^{+7.7}_{-10.5}$	7.9 $^{+5.5}_{-0.0}$	-1.41 $^{+0.11}_{-0.25}$	1.5 $^{+0.7}_{-0.0}$	13.9	1
1232	dE	184.1771	6.6895	NGC4215	32.0	18.9	6.4	0	0	2086.6 $^{+3.9}_{-4.1}$	10.7 $^{+2.3}_{-1.8}$	-1.49 $^{+0.07}_{-0.08}$	2.1 $^{+0.1}_{-0.5}$	26.0	1
320	dE	72.4170	-4.2329		14.0	20.6	4.1	0		960.2 $^{+15.1}_{-12.6}$	6.9 $^{+2.4}_{-0.1}$	-2.21 $^{+0.15}_{-0.0}$	1.2 $^{+0.2}_{-0.0}$	6.7	0
318	dE	72.1070	-3.8733	PGC016060	38.0	20.3	3.7	0	0	2803.0 $^{+9.2}_{-11.6}$	11.4 $^{+1.7}_{-3.0}$	-1.69 $^{+0.1}_{-0.28}$	1.1 $^{+1.0}_{-0.4}$	11.6	1
585	dE	146.4547	-0.5469	IC0560	27.0	18.8	11.7	1	0	1832.9 $^{+12.8}_{-9.2}$	9.0 $^{+2.9}_{-3.1}$	-1.88 $^{+0.17}_{-0.13}$	1.1 $^{+0.7}_{-0.0}$	14.2	1
578	dE	146.2100	0.1444		92.0	19.6	6.1	1	1	6463.2 $^{+22.1}_{-33.7}$	6.2 $^{+7.4}_{-0.2}$	-2.07 $^{+0.15}_{-0.15}$	1.2 $^{+0.8}_{-0.0}$	13.8	1
218	dEN	42.9988	-1.1746		100.0	17.5	8.8	0	1	6988.7 $^{+2.3}_{-1.8}$	9.6 $^{+2.3}_{-0.0}$	-0.72 $^{+0.07}_{-0.05}$	2.3 $^{+0.4}_{-0.0}$	25.7	1
428	dEN	133.6689	-3.1090	NGC2695	32.0	19.7	5.2	0	0	2164.3 $^{+10.2}_{-12.0}$	10.6 $^{+2.4}_{-3.0}$	-1.28 $^{+0.22}_{-0.18}$	1.5 $^{+0.8}_{-0.0}$	11.2	1
429	dE	133.7407	-2.9390	NGC2695	32.0	21.2	3.0	0	0	1677.5 $^{+44.1}_{-36.4}$	8.1 $^{+2.3}_{-3.6}$	-1.8 $^{+0.26}_{-0.47}$	1.7 $^{+0.1}_{-0.7}$	4.9	1
420	dE	133.3598	-2.5094	NGC2695	32.0	19.0	4.6	1	0	1869.1 $^{+5.3}_{-12.7}$	8.6 $^{+2.8}_{-0.8}$	-1.76 $^{+0.07}_{-0.15}$	1.5 $^{+0.3}_{-0.1}$	18.1	1

Continued on next page

Table A.1: (Continued) Properties of the dwarf galaxies studied in this work.

ID	Morph	RA	Dec	Host	D	M_g	R_{eff}	Em	Bkg	V	Age	[M/H]	ML	SNR	Q
(1)	(2)	[deg]	[deg]	(5)	[Mpc]	[mag]	["]	(9)	(10)	[km/s]	[Gyr]	[dex]	(14)	(15)	(16)
544	dE	145.1226	5.2314	NGC2962	34.0	19.1	5.4	1	0	2123.7 ^{+13.4} _{-1.5}	9.9 ^{+2.7} _{-2.1}	-1.79 ^{+0.11} _{-0.13}	1.1 ^{+0.8} _{-0.3}	17.3	1
645	dE	153.3468	3.3098	NGC3156	22.0	19.7	6.4	0	0	1394.6 ^{+13.4} _{-7.4}	9.8 ^{+2.5} _{-3.0}	-1.49 ^{+0.19} _{-0.18}	1.7 ^{+0.3} _{-0.4}	10.8	1
652	dEN	153.6326	3.3670	NGC3156	22.0	17.6	10.1	0	0	1246.6 ^{+2.3} _{-2.1}	8.9 ^{+2.3} _{-1.2}	-1.27 ^{+0.08} _{-0.03}	1.6 ^{+0.3} _{-0.2}	37.1	1
642	dE	153.1371	3.7079	NGC3156	22.0	19.3	4.4	0	0	1121.2 ^{+4.9} _{-3.8}	11.9 ^{+1.6} _{-2.2}	-1.63 ^{+0.1} _{-0.11}	2.2 ^{+0.1} _{-0.6}	22.2	1
928	dE	169.8325	2.7918	NGC3640	26.0	18.2	8.5	0	0	1551.1 ^{+6.9} _{-6.4}	11.3 ^{+2.7} _{-1.6}	-1.75 ^{+0.09} _{-0.15}	1.8 ^{+0.3} _{-0.2}	16.6	1
974	dE	170.4586	2.9454	NGC3641	26.0	19.3	4.8	0	0	1844.5 ^{+5.1} _{-3.6}	10.0 ^{+1.7} _{-1.9}	-1.61 ^{+0.13} _{-0.11}	1.4 ^{+0.5} _{-0.1}	22.3	1
992	dE	170.7233	3.2479	NGC3640	26.0	17.9	6.7	0	0	1431.0 ^{+2.7} _{-2.1}	13.9 ^{+0.0} _{-0.1}	-1.49 ^{+0.01} _{-0.0}	2.2 ^{+0.0} _{-0.0}	44.0	1
1400	dE	190.2123	7.9309	NGC4623	17.0	17.1	16.2	0	0	2162.6 ^{+2.1} _{-1.7}	11.3 ^{+0.7} _{-2.7}	-1.2 ^{+0.07} _{-0.06}	2.0 ^{+0.1} _{-0.3}	31.8	1
829	dE	164.2337	9.4990		148.0	20.0	3.9	1	1	10366.3 ^{+22.0} _{-2.1}	6.6 ^{+3.4} _{-0.5}	-1.77 ^{+0.13} _{-0.13}	1.7 ^{+0.2} _{-0.6}	11.8	1
2103	dE	239.0837	6.1882	NGC6017	29.0	18.0	14.2	1	0	1735.4 ^{+6.0} _{-8.4}	11.3 ^{+2.2} _{-2.5}	-1.69 ^{+0.01} _{-0.22}	1.5 ^{+0.6} _{-0.1}	20.1	1
1793	dEN	213.4112	-3.3354	NGC5507	28.0	19.4	6.4	0	0	1863.3 ^{+7.0} _{-6.1}	12.7 ^{+1.3} _{-1.6}	-1.55 ^{+0.03} _{-0.12}	2.0 ^{+0.2} _{-0.2}	16.7	1
20	dEN	19.5843	3.4333	NGC0474	31.0	20.7	4.5	0	0	2409.8 ^{+15.8} _{-13.4}	12.6 ^{+0.9} _{-2.1}	-1.7 ^{+0.17} _{-0.28}	2.2 ^{+0.0} _{-0.4}	9.1	1
1497	dE	191.8999	-1.6508	NGC4690	40.0	21.0	4.3	0	0	2634.9 ^{+15.8} _{-16.5}	8.5 ^{+2.6} _{-2.7}	-1.26 ^{+0.22} _{-0.23}	1.2 ^{+0.8} _{-0.1}	6.0	0
1781	dEN	212.7999	-5.1036	NGC5493	39.0	18.6	5.8	1	0	2763.9 ^{+0.1} _{-22.9}	7.3 ^{+4.1} _{-0.3}	-2.1 ^{+0.11} _{-0.11}	1.2 ^{+0.3} _{-0.0}	17.0	1
2086	dEN	226.8657	1.3651	NGC5845	25.0	19.4	6.6	0	0	1379.6 ^{+5.8} _{-5.8}	8.4 ^{+3.6} _{-1.0}	-1.49 ^{+0.1} _{-0.14}	1.6 ^{+0.4} _{-0.2}	17.4	1
2088	dE	226.8973	1.9944	NGC5839	22.0	19.8	4.8	0	0	1172.1 ^{+6.0} _{-6.4}	12.2 ^{+1.5} _{-3.4}	-1.42 ^{+0.12} _{-0.07}	2.0 ^{+0.2} _{-0.3}	17.6	1
2091	dEN	227.0116	2.2354	NGC5845	25.0	19.2	8.2	0	0	1436.3 ^{+6.3} _{-5.7}	10.9 ^{+1.3} _{-2.2}	-1.82 ^{+0.13} _{-0.12}	1.5 ^{+0.5} _{-0.1}	18.9	1
2098	dE	238.7639	0.4664	NGC6010	31.0	19.0	4.3	1	0	1814.8 ^{+5.0} _{-2.8}	10.3 ^{+1.3} _{-2.2}	-1.68 ^{+0.09} _{-0.1}	1.3 ^{+0.6} _{-0.3}	31.1	1
2094	dE	238.3115	0.7097	NGC6010	31.0	18.4	8.3	0	0	2057.0 ^{+4.7} _{-6.4}	8.2 ^{+4.2} _{-0.8}	-1.83 ^{+0.14} _{-0.16}	1.5 ^{+0.4} _{-0.1}	17.4	1
1393	dEN	189.9051	-4.8152	NGC4602	34.0	19.3	4.8	1	0	2452.3 ^{+8.5} _{-3.7}	9.4 ^{+1.3} _{-1.2}	-1.56 ^{+0.06} _{-0.09}	1.7 ^{+0.1} _{-0.2}	24.2	1

Note. Column (1): MATLAS ID of dwarf galaxies. Dwarfs identified in the MATLAS survey are numbered from 1 to 2210, e.g., MATLAS-2019. Column (2): morphology of the dwarf galaxy. Column (3): right ascension in degrees. Column (4): declination in degrees. Column (5): assumed host galaxy based on minimal difference in line-of-sight velocities between satellite and massive host. Column (6) distance of the assumed host if present. If no host could be assigned, the distance results from the dwarf recessional velocity via Hubble's law. Column (7): Absolute g -band magnitude. We use the apparent g -band magnitude from Poulain et al. (2021) and the distance from column (6). Column (8): Effective radius in arcseconds via GALFIT modelling from Poulain et al. (2021). Column (9): emission line flag. Values 1 for emission lines present, 0 for no emission lines. Column (10): background flag. Values 1 if the dwarf galaxy resides outside of the ATLAS^{3D} target volume and 0 if it lies inside. This is based on the dwarf line-of-sight velocity compared with the velocities of the massive ATLAS^{3D} galaxies (see Figure 6). Column (11): dwarf line-of-sight velocity in km/s. Column (12): dwarf age in Gyr. Column (13): dwarf metallicity in dex. Column (14): stellar mass-to-light ratio in the V -band. Column (15): signal-to-noise ratio of the continuum spectrum. Column (16): quality of the spectrum. Values 1 for clear spectral lines, 0 if the noise dominates the lines and the measured values are uncertain.